Elastic Scattering of Gaussian Beams from Microspheres

by

Abdullah Demir

A Thesis Submitted to the
Graduate School of Sciences and Engineering
in Partial Fulfillment of the Requirements for
the Degree of

Master of Science

in

Computational Science and Engineering

Koc University

July 2005

Koc University

Graduate School of Sciences and Engineering

This is to certify that I have examined this copy of a master's thesis by

Abdullah Demir

and have found that it is complete and satisfactory in all respects,
and that any and all revisions required by the final
examining committee have been made.

Committee Members:

_____

Ali Serpengüzel, Ph. D. (Advisor)

_____

Mine Çağlar, Ph. D.

_____

Alper Kiraz, Ph. D.

Date: _____

ABSTRACT

Microspheres have received increasing attention as optical microcavity resonators due to their high quality Morphology Dependent Resonances (MDRs). Numerous applications have been realized by using microsphere MDRs in photonics, optoelectronics, and optical communication systems. Wavelength selective properties of resonances in microspheres have been used as a building block for filtering, multiplexing, switching, and channel dropping applications. Microsphere based biosensors has been attracting the attention of the photonics community due to their high sensitivity, selectivity and implementation. Adsorption of different biomolecules on the surface of microspheres causes a change of effective size and refractive index leading to the shift of resonance wavelengths. A photonic biosensor, based on this phenomenon, can detect a single molecule sensitively depending on the configuration.

In this work, rainbow effects on microspheres are studied numerically by using Generalized Lorenz Mie Theory (GLMT). GLMT description of Gaussian beam scattering by a microsphere is an excellent analytical tool to accurately model the sphere-Gaussian-beam interaction. Angularly resolved Gaussian beam scattering spectra are presented to observe the effect of rainbows on MDRs. Obtained results show that rainbows give rise to increased scattering intensity around MDRs. Phase behavior of the total scattered field is observed in the spectra around rainbow angles. The rainbow-enhanced MDRs and associated phase characteristics provide an additional enhancement of the already sharp MDRs of microspheres for sensing applications.

ACKNOWLEDGEMENTS

First and foremost, I would like to thank my academic advisor, Professor Ali Serpengüzel, for the support and guidance he has provided me throughout my study.

I would like to thank Prof. Mine Çağlar and Prof. Alper Kiraz for reading my thesis and providing constructive feedback.

During my thesis work, I have enjoyed interacting with other graduate students of my group, İbrahim İnanç, Yiğit Ozan Yılmaz, Bora Akçay, Onur Akatlar, Filiz Ateş, and Ulaş Kemal Ayaz. In particular I have enjoyed working and sharing ideas with Adnan Kurt.

Outside of my group, I would like to thank my friends, for their friendship. I am fortunate to have met Kamil Varol, Ümit Demirbaş, and Şennur Turgut.

In addition, I wish to thank my family, for their support, love and patience during my entire time at Koç University. It is to them, I wish to dedicate this thesis.

TABLE OF CONTENTS

List of Tables vii

List of Figures viii

Nomenclature xi

Chapter 1: Introduction 1

Chapter 2: Optical Resonators 3

2.1 Introduction. . . . 3

2.2 The Fabry-Perot Resonator. . . . 3

2.2.1 Resonator Modes. . . . 4

2.2.2 Phase and Intensity of Resonances. . . . 9

2.2.3 Superposition of Fields. . . . 12

Chapter 3: The Microsphere Resonator 14

3.1 Microsphere . . . 14

3.2 Lorenz Mie Theory. . . . 15

3.3 Properties of MDRs . . . 18

3.3.1 Q-factor. . . . 18

3.3.2 Mode Spacing . . . 19

3.3.3 Mode Position . . . 21

3.4 Excitation of MDRs . . . 21

3.4.1 Gaussian Beam Excitation. . . . 22

3.4.2 Generalized Lorenz Mie Theory . . . 24

3.4.3 Excitation Efficiency of MDRs . . . 26

Chapter 4: Rainbow Effect on Resonances **28**
4.1 Geometrical Optics. 28
4.1.1 Gaussian Beam Excitation Geometry 30
4.1.2 Rainbow Enhanced Scattering. 32
4.2 Scattered Field Intensity 34
4.2.1 Rainbow Enhanced Scattering. 38
4.2.2 TE Component. 39
4.2.3 TM Component 42
4.2.4 Phase Effect on MDRs. 44

Chapter 5: Applications of Microspheres **46**
5.1 Biomolecular Detection Applications 46
5.1.1 Perturbation Approach. 47
5.1.2 Numerical Results 49
5.2 Infrared Light Scattering 54

Chapter 6: Conclusion **57**

Appendix A **58**

Vita **66**

Bibliography **67**

LIST OF TABLES

3.1 Summary of Notation. 16

A.1 Average and maximum percent error of the Maxwell's equations for zeroth- to fifth-order Gaussian beam description. 63

LIST OF FIGURES

2.1 The schematic Fabry-Perot resonator. 5

2.2 Transmitted light intensity of the resonator modes. 7

2.2 The mode spacing for Fabry-Perot resonator with m = 1.5 and m = 3.5 8

2.3 (a)Transmitted and (b)reflected light intensity for a Fabry-Perot resonator. As the reflectance R decreases, the intensity at the minima increases. 11

2.4 Transmission intensity for addition of two fields in a Fabry-Perot resonator . . . 13

2.5 Phase-induced transmission intensity for addition of two fields in a Fabry-Perot resonator 13

3.1 The microsphere of radius a and refractive index m. 15

3.2 Internal intensity distribution in the equatorial plane for TE MDR with n=12, l=2 16

3.3 Effect of shape deformation on the emission from various regions of sphere rim 17

3.4 The MDRs and mode spacing $\Delta\lambda$ between consecutive modes 20

3.5 The mode spacing for Fabry-Perot and microsphere resonator with m = 1.5 and m = 3.5 20

3.6 Paths of MDRs and focused spots for a plane wave illumination of microspheres. 21

3.7 Gaussian beam excitation geometry of microspheres. 23

4.1 Ray representation of MDRs and rainbows(for three internal reflections). 29

4.2 Geometrical optics picture of the incident and scattered rays 31

4.3 Periodic rainbow formation geometries for n_R = 3, 4, 5 and 6 for edge excitation. 33

4.4 Refractive index (m) of a sphere as a function of periodic rainbow reflections . . 34

4.5 Electric field of the background(rainbow) field(E_B) and MDR field (E_M) 35

4.6 Superposition of rainbow (EB) and MDR field (EM) results in three possible phase-induced scattering intensity. 37

4.7 Expected spectra for the superposition of rainbows and MDRs for a sphere with m =2 (three horizontal bars show the three possible rainbow angles around $\theta = \pm 120^o$ and 0^o) 39

4.8 Low resolution color image of the intensity of transverse electric (TE) elastic light scattering from a microsphere with a radius of 10.00μm and refractive index of m = 2. 40
4.9 High resolution color image of the TE light scattering intensity with wavelength resolution of 0.001 nm and angle resolution of 0.2^{o}. The spectra shows (a) Angle-oriented scattering intensity for a low Q-factor MDR (b) Wavelength-oriented scattering intensity for a high Q-factor MDR. 41
4.9 Low resolution color image of the intensity of transverse magnetic (TM) elastic light scattering from a microsphere with a radius of 10.00 μm and refractive index of m = 2 42
4.11 High resolution color image of the TM light scattering intensity with wavelength resolution of 0.001 nm and angle resolution of 0.2^{0} a)Angle-oriented scattering intensity for a low Q-factor MDR b)Wavelength-oriented scattering intensity for a high Q-factor MDR 43
4.12 Phase-induced TE scattering intensity for a MDR around 1^{st} order rainbow. . . . 44
4.13 Phase induced TM scattering intensity for a MDR around 1^{st} order rainbow . . . 45
5.1 Biomolecular detection by Fabry-Perot resonator 46
5.2 Scheme of the molecular adsorption on microsphere surface. 47
5.3 Elastic light scattering geometry from a microsphere for biomolecular detection . 50
5.4 Expected elastic light scattering in the 0^{o} (transmission) and the 90^{o} spectra for the configuration in fig 5.2 50
5.5 a) Transverse electric (TE) elastic light scattering spectra from a silica microsphere with a radius of 20.00 μm and 20.01 μm b) High resolution TE elastic light scattering spectra from a silica microsphere with a radius of 20.00 μm and 20.01 μm. 52
5.6 a) Transverse magnetic (TM) elastic light scattering spectra from a silica microsphere with a radius of 20.00 μm and 20.01 μm b) High resolution TM elastic light scattering spectra from a silica microsphere with a radius of 20.00 μm and 20.01 μm 53

5.7. Transverse electric (TE) elastic light scattering spectra of CO_2 laser beam from a silicon microsphere with a radius of 250 μm 55
5.8. Transverse electric (TE) elastic light scattering spectra of CO_2 laser beam from a silicon microsphere with a radius of 250 μm 55

NOMENCLATURE

a	microsphere radius
a_n	elastically scattered transverse magnetic field coefficient
b_n	elastically scattered transverse electric field coefficient
c_n	internal transverse magnetic field coefficient
d_n	internal transverse electric field coefficient
$\Delta\lambda$	mode spacing in wavelength
$\delta\lambda$	wavelength shift
ε	permittivity of the medium
E	electric field amplitude
$\hbar$	Plank's constant divided by 2π
$h_n^1(x)$	spherical Hankel function of the first kind
$h_n^2(x)$	spherical Hankel function of the second kind
$j_n(x)$	spherical Bessel function
k	wavenumber
L	spreading length
l	mode order
λ	wavelength
$\lambda_{1/2}$	linewidth of an MDR in wavelength
m	azimuthal mode number
m	refractive index of the sphere
s	beam confinement parameter
μ	Permeability of the medium
n	Mode number
ω	Optical angular frequency

$\omega_{n,l}$	resonant angular frequency
p	momentum of the photons
P_i	power coupled into MDR
Q	quality factor of a MDR
Q_0	quality factor associated with the internal losses
$Q_{coupling}$	quality factor associated with the coupling losses
Q_{abs}	quality factor associated with the absorption losses
Q_r	quality factor associated with the diffraction leakage losses
Q_s	quality factor associated with the scattering losses
σ_{mode}	scattering cross section of an MDR
$<\sigma>$	coupling efficiency of a Gaussian beam
θ	polar angle
$\Delta\theta$	spreading angle of rainbow
θ_{in}	angle of incidence
θ_c	critical angle
x	size parameter of microsphere

Chapter 1

INTRODUCTION

Microspheres are special due to their high quality factor (Q-factor) morphology dependent resonances (MDR's), i.e., whispering gallery modes (WGM's) [1 ,2] with reported Q-factors as large as $2x10^{10}$ [3]. A variety of potential applications have been established by using dielectric microspheres such as microlasers [4], channel dropping filters [5,6] optical switches [7], ultrafine sensors,[8] biomolecular agent detectors [9,10], displacement sensors [11], rotation detectors [12], high-resolution spectrometers [13], and Raman lasers [14]. More recently, silicon microspheres have been used in elastic light scattering and optical channel dropping [15]

Additionally, the field of optical biosensors is rapidly evolving due to the need to overcome the limitations of the amount of material to be detected [16]. Optical microsphere resonators with high Q-factor MDR's can be used as sensitive biodetectors. These extraordinary Q-factors, translate directly to high energy density and narrow resonant-wavelength lines [17]. The sharp optical resonance of microsphere provides exceptional resolving power, down to submonolayer molecular level. A biomolecule such as a protein that resides in the evanescent field of MDR's can absorb light, thus influencing the MDR's [18]. By affixing the appropriate proteins and DNA molecules to the surface of the microsphere, and measuring the Q-factor and observed shift in the resonant peak locations, the biomolecules sticking to the surface can be characterized [19]. The shift of MDR's by protein adsorption onto microspheres is demonstrated and modeled as a first order perturbation [4]. Recently, the red shift of resonance wavelengths is used for high sensitivity label-free DNA quantification [20].

Focused off-axis illumination of a sphere is necessary to increase the coupling strength leading to higher power transfer into the microsphere, which is essential for filtering applications in optical-fiber communication, optical switching, and cavity QED [21]. Excitation efficiency of MDRs by Gaussian beams is higher than that of plane-waves [22]. In addition to the rigorous Lorenz-Mie theory to predict the interaction of light with a sphere, the basis of some of the observed effects can be

identified from the geometry of rays refracted by the sphere. Plane-wave illumination of spheres confirmed the existence of scattering enhancement associated with the rainbows for spheres of specific refractive indices at specific angles [23].

Contrary to MDRs, rainbows are independent of the microsphere size and depend only on refractive index and incident angle of the ray. If a ray refracted into the sphere returns to its initial position after reflections from the surface, then a finite number of rainbow angles form since the ray will follow the same path in the subsequent reflections. For example, with a sphere of refractive index m = 2, a ray comes to its initial position after reflections inside the sphere, and only three rainbows form in the scattering intensity. Periodic rainbow formation is ideal to understand the effect of rainbows on MDRs around rainbow angles.

Chapter 2 provides a necessary overview on Fabry Perot resonators that gives a basic description of optical resonances. The characteristics of the Fabry-Perot resonators can be extended further in the analysis of microsphere MDRs.

Chapter 3 describes the MDRs of microspheres using Lorenz Mie theory of plane-wave and Generalized Lorenz Mie Theory description of focused Gaussian beam scattering. Essential features of MDRs such as position, mode spacing, and Q-factor, are overviewed. Excitation of resonances with plane wave and Gaussian beams and their associated excitation efficiencies are analyzed.

Chapter 4 is on rainbows, using the ray picture of scattering from spheres. Rainbow effect on MDRs are described that rainbows give rise to increased sensitivity of scattering intensity around MDRs.

Chapter 5 explores the applications of microspheres, with emphasis on biomolecular detection. In addition, infrared light scattering is studied for optical channel dropping.

The thesis is concluded with a short summary of the performed study.

Chapter 2

OPTICAL RESONATORS

2.1. Introduction

In an optical resonator light circulates (or is repeatedly reflected) within the system, with small loss. Optical resonators are used mainly to build up large field intensities with moderate input powers. The Fabry-Perot resonator consists of two or more planar or curved surfaces to trap an optical beam by multiple reflections [24]. The corresponding wavelength (frequency) of the beam is called the mode of the resonator (resonance wavelength). Planar and spherical mirror resonator, ring resonator, and optical-fiber resonator are the most typical optical resonators. In addition to the one- and two-dimensional optical resonators, microsphere resonators confine light in three-dimensions. The general condition for all resonators is that phase matching should be satisfied in a round-trip of the resonator, such that the phase shift imparted by a single round trip of propagation should be a multiple of 2π, i.e.,

$$\Delta\phi = 2\pi n, \tag{2.1}$$

for an integer mode number n. The resonances occur when there is an integer mode number (n) of half-wavelengths. The waves satisfying the condition of phase matching interferes constructively which results in a series of standing electromagnetic waves. The corresponding modes of phase matching determine the wavelengths (or frequencies) of the resonator. These modes store radiation energy only at the wavelengths of the modes.

2.2. The Fabry-Perot Resonator

The simplest resonator consists of two parallel planar mirrors, called Fabry-Perot resonator [24]. The Fabry-Perot resonator with fixed resonator spacing is called an etalon, and if the plate

separation is variable, it is called an interferometer. The Fabry-Perot resonators selectively reflect or transmit a particular wavelength of light. To understand the operation principle of a Fabry-Perot resonator, let us analyze first a single plate with reflectance R. If a plane-wave is incident on a single plate with reflectance R = 99.9 %, almost no light passes through the plate. However, if two of these plates are placed parallel to each other, something surprising occurs. The plates become transparent at particular wavelengths because of multiple reflections within the resonator. The light bounces back and forth between the plates and only a small percentage of light passes through the plates at each bounce. The transmitted light from each pass interferes constructively with other passes, for the special case of in phase arrival of each wave. Therefore, the total transmitted light through the resonator becomes 100% at these particular wavelengths of light, independent of the value of R. These wavelengths of the incident light satisfying the resonance condition in eq. (2.1) are called the resonance wavelengths.

2.2.1. Resonator Modes

The resonator modes are the wavefunctions and resonance wavelengths (frequencies) of the optical waves that exist self-consistently within the resonator. The modes of a resonator are the solutions of the Helmhotz equation subject to the appropriate boundary conditions. A mode is a self-reproducing wave that interferes with itself constructively after a single round-trip between the mirrors with spacing d and refractive index m. Therefore, only self-reproducing waves or combinations of them can exist within the resonator in the steady state. Standing wave solutions for a Fabry Perot resonator restricts the resonance wavelengths to discrete values; therefore the half-wavelength of the *n*th order resonance should fit in the spacing between the plates such that

$$n\frac{\lambda_n}{2} = md\ , \tag{2.2}$$

where md is the effective spacing of the plates. We can define a dimensionless size parameter (x) as the ratio of the round-trip path length to the wavelength of the incident light,

$$x = \frac{2d}{\lambda}. \tag{2.3}$$

Then, the resonant size parameter of the resonator with mode order *n* can be written as

$$mx = n, \qquad n = 1, 2, 3, \ldots \tag{2.4}$$

as a function of size parameter and internal refractive index of the resonator. The waves satisfying the phase matching condition of eq. (2.1) interfere constructively, which results in a series of standing electromagnetic waves given by eq. (2.4). Any change in refractive index or surface spacing of the resonator results in different resonance wavelengths. The shift in a resonance wavelength is given by

$$\delta\lambda = \lambda\left(\frac{\delta d}{d} + \frac{\delta m}{m}\right), \tag{2.5}$$

which is a function of thickness d and refractive index m of the resonator. Therefore, any change in m or d leads to shifted resonator modes, which makes Fabry-Perot interferometer a sensitive device for wavelength selectivity.

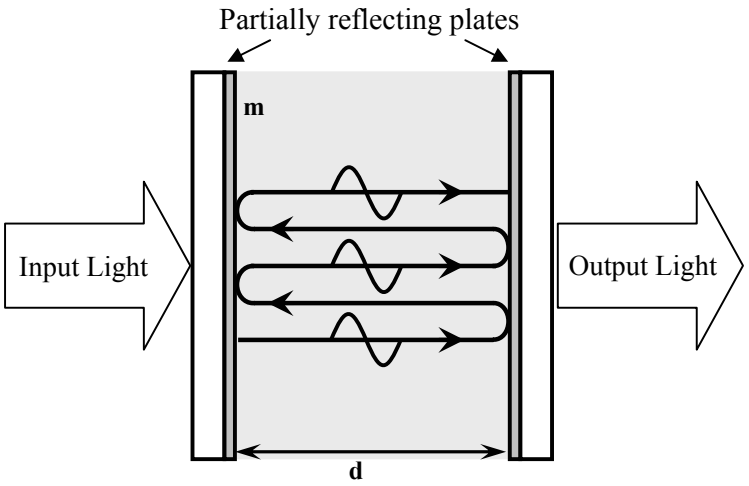

Figure 2.1. The schematic Fabry-Perot resonator.

At these resonance wavelengths, the resonator transmits 100% of the input beam regardless of the reflectance of the plates. Although R does not effect the peak transmittance, the value of R does effect the sharpness of the plates. A measure of this property is the quality factor (*Q-factor*) of the resonator, defined by the relation

$$Q = 2\pi \frac{stored\ \ energy}{energy\ \ loss\ \ per\ \ cycle}, \tag{2.6}$$

which is identical to the ratio of the wavelength to the half-width of the resonance

$$Q = \frac{\lambda}{\Delta\lambda_{1/2}}, \tag{2.7}$$

or

$$Q = \frac{\upsilon}{\Delta\upsilon_{1/2}}, \tag{2.8}$$

in frequency domain. Both eqs. (2.7) and (2.8) defines the sharpness of the resonance and they are also called the resolving power of the resonator. The larger the value of R is, the sharper the resonance, which makes the Fabry-Perot resonator applicable as a tool for selecting a particular wavelength of light. In some applications, such as in a laser cavity or a monochromator, high Q-factor peaks are more desirable.

There is an infinite number of resonator mode satisfying resonance condition, in which the resonance wavelengths are separated by a distance called free spectral range (FSR) or mode spacing. In the Fabry-Perot interferometer, FSR can be perceived as the maximum width of the spectrum that can be determined without ambiguity. The distance between adjacent resonances has consecutive mode number such that FSR can be defined as

$$\Delta\lambda_{FSR} = \frac{\lambda_n}{n} - \frac{\lambda_{n+1}}{n+1}, \tag{2.9}$$

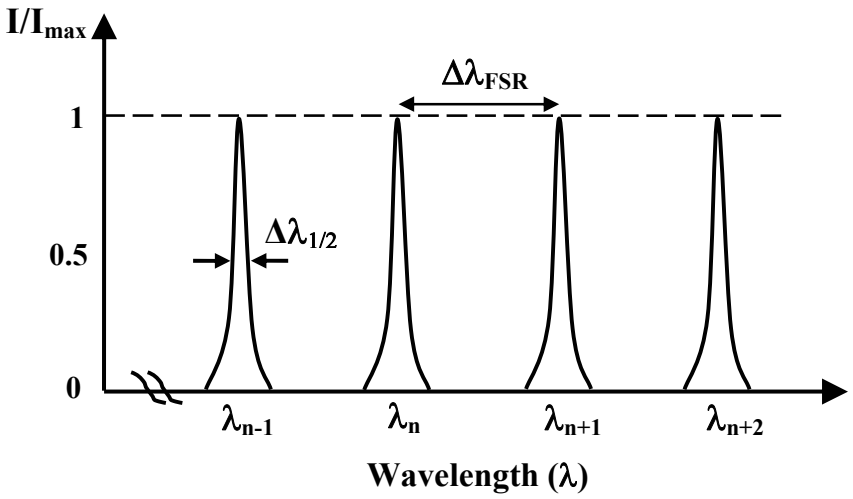

Figure 2.2. Transmitted light intensity of the resonator modes.

and by using eq. (2.2) and $n \approx n+1$ for large mode orders n,

$$\Delta\lambda_{FSR} = \frac{2md}{n} - \frac{2md}{n+1} = \frac{2md}{n(n+1)} \cong \frac{2md}{n^2} = \frac{\lambda^2}{2md}, \tag{2.10}$$

around wavelength λ. In terms of frequency, the free spectral range (FSR) is

$$\Delta\upsilon_{FSR} = \frac{c}{\lambda^2}\Delta\lambda_{FSR} = \frac{c}{2md}, \tag{2.11}$$

The approximations in eqs. (2.10) and (2.11) become better as n gets larger. The FSR decreases when the distance between the plates increases. Similar to the *Q-factor* of the resonator defined in eq. (2.7), the ratio of the FSR to the resonant linewidth, i.e.

$$F = \frac{\Delta\lambda_{FSR}}{\Delta\lambda_{1/2}} = \frac{\Delta\upsilon_{FSR}}{\Delta\upsilon_{1/2}}, \tag{2.12}$$

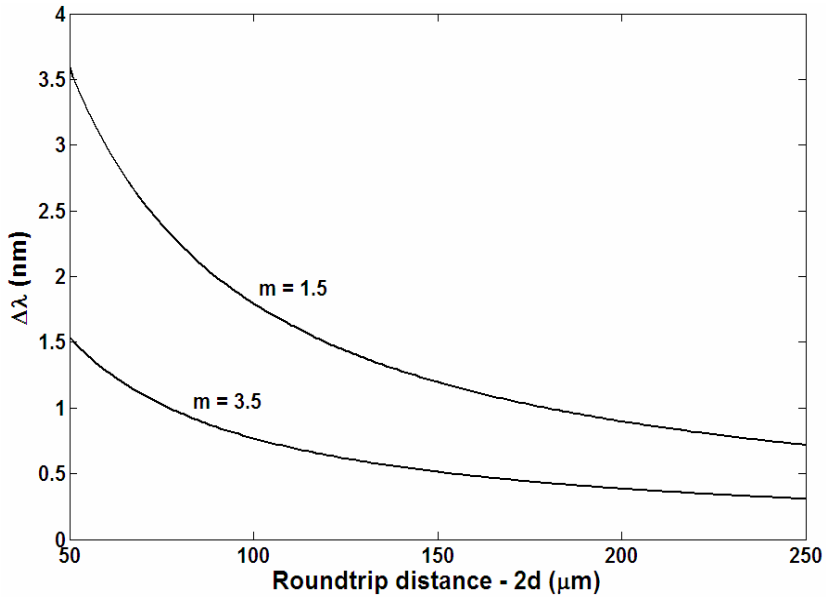

Figure 2.3. The mode spacing for Fabry-Perot resonator with m = 1.5 and m = 3.5.

is called the *finesse* of the resonator, which is equal to

$$F = \frac{\pi\sqrt{R}}{1-R} \tag{2.13}$$

for a Fabry-Perot resonator. The *finesse* increases with an increase in R. Using the definitions in eq. (2.7) for *Q-factor* and (2.12), (2.13) for *finesse* with the value of FSR in eq. (2.10), the Q-factor for a Fabry-Perot resonator is found to be,

$$Q = \frac{\lambda}{\Delta\lambda_{FSR}} F = nF = \frac{2md\pi\sqrt{R}}{\lambda(1-R)} = \frac{mx\pi\sqrt{R}}{1-R}, \tag{2.14}$$

which is a function of internal refractive index, size parameter of the resonator and reflectance of the surfaces. As one of these parameters increases, the Q-factor of the resonator becomes larger, leading to sharper resonances. Increasing the resonator size and refractive index requires waves with larger

mode numbers (since $mx = n$); therefore, higher order modes leads to high *Q-factor* resonances. Also, increasing the reflectance (R) of the surfaces results in higher *Q-factor* resonances.

2.2.2. Phase and Intensity of Resonances

In a Fabry Perot resonator, multiple beams interfere constructively to form a resonance such that the net result is the superposition of an infinite number of waves, separated by equal phase delays δ. Phase delay is due to the difference in optical path length between the successive transmitted waves that superpose to form a resonance. The difference in optical path length between adjacent waves with normal incidence on the plates is given by

$$\delta = (2md)k_0 = mxk_0 = \frac{2md\pi}{\lambda} = mx\pi\,, \tag{2.15}$$

where k_0 is the wavenumber of the incident beam. The amplitude of the transmitted field is the sum of the amplitudes of all the transmitted components.

If $E_0e^{i\omega t}$ is the incident wave, the total transmitted field E_t is represented by the sum of the transmitted waves after reflections and transmissions [25],

$$\begin{aligned} E_t &= E_{1t} + E_{2t} + E_{3t} + \ldots + E_{Nt}\,, \\ &= E_0t^2e^{i\omega t} + E_0t^2r^2e^{i(\omega t-\delta)} + E_0t^2r^4e^{i(\omega t-2\delta)} + \ldots + E_0t^2r^{2(N-1)}e^{i[\omega t-(N-1)\delta]}, \\ &= E_0Te^{i\omega t}\left[1 + \mathrm{Re}^{-i\delta} + R^2e^{-i2\delta} + \ldots + R^{(N-1)}e^{-i(N-1)\delta}\right], \end{aligned} \tag{2.16}$$

where r is the reflection and t is the transmission amplitude coefficients of the resonator surfaces. The square of transmission and reflection amplitudes are called the transmittance (T) and reflectance (R) of the surfaces such that in the case of no absorption T+R=1. For an infinite number of waves the transmitted field is given by

$$E_t = E_0e^{i\omega t}\left[\frac{T}{1-\mathrm{Re}^{i\delta}}\right]. \tag{2.17}$$

The distance between resonances corresponds to change in δ of 2π. A general representation of a field is written as

$$E = E_0 e^{i(\omega t+\phi)} = E_0 e^{i\omega t} e^{i\phi} \tag{2.18}$$

including a phase ϕ of the amplitude. Comparing eq. (2.17) and (2.18) results in

$$e^{i\phi} = \left[\frac{T}{1-\mathrm{Re}^{i\delta}}\right], \tag{2.19}$$

which leads to

$$\tan\phi = \mathrm{Im}\left[\frac{T}{1-\mathrm{Re}^{i\delta}}\right] \Big/ \mathrm{Re}\left[\frac{T}{1-\mathrm{Re}^{i\delta}}\right], \tag{2.20}$$

and the phase factor of the transmitted field is found to be

$$\phi = \tan^{-1}\left(\frac{\sin\delta}{1/R-\cos\delta}\right), \tag{2.21}$$

which is a function of path difference and reflectance. The resonances occur when the phase delay is a multiple of 2π.

Once the field inside the resonator is known, the corresponding intensity of the transmitted light can be found from square modulus E·E*. The output intensity will be a fraction of the input intensity. The amount of transmitted light is determined by the reflectance R. A fraction of the incident light (1-R) will enter the cavity as $I_{incident}$, of which part (again 1-R) will leave the cavity as $I_{transmitted}$. Thus the ratio of transmitted to incident light is given by

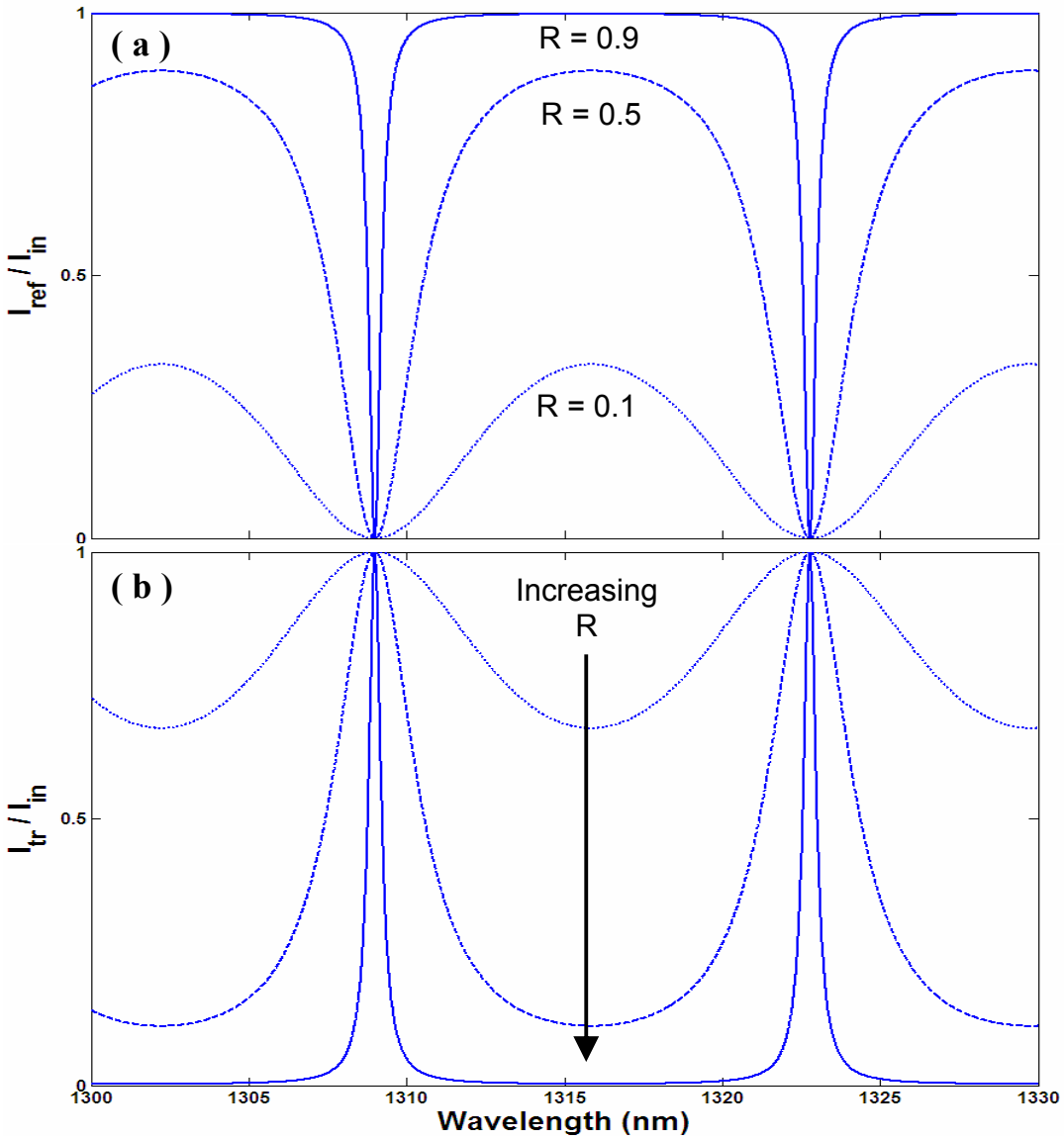

Figure 2.4. (a) Transmitted and (b) reflected light intensity for a Fabry-Perot resonator. As the reflectance R decreases, the intensity at the minima increases.

$$\frac{I_t}{I_0} = \frac{1}{1 + \frac{4R}{(1-R)^2}\sin^2(\delta/2)}. \tag{2.22}$$

The transmitted light intensity is maximum at the location corresponding to a phase change of 2π, called resonance wavelengths. As shown in fig. 2.4, the higher the reflectance (R), the lower the intensity at the minima and the sharper the transmitted intensity at the maxima. The reflected light intensity can be found using eq.(2.22) as

$$\frac{I_R}{I_0} = \frac{I_0 - I_t}{I_0} = \frac{2R(1-\cos\delta)}{(1+R^2) + 2R\cos\delta}. \tag{2.23}$$

2.2.3. Superposition of Fields

Addition of two fields of different phases leads to interesting effect in transmission spectrum of Fabry-Perot resonators. Let one of the field has a phase delay of 1/k of the other field. Therefore, the interference of two fields will have a transmitted field which is given by eq. 2.17, neglecting the time part, as

$$E_t = E_0\left[\left(\frac{T}{1-\mathrm{Re}^{i\delta}}\right) + e^{i\delta/k}\right]. \tag{2.24}$$

The behavior of such a field does not change the resonance wavelengths but spread the transmission of resonances around some k values. Although light should be transmitted thoroughly at resonance wavelengths independent from reflectance (R), we observe almost-zero transmission regions for some k values. The behavior of adding two fields is shown in fig. 2.5, as a function of k-factor, for R=0.9. The phase in the intensity spectrum can be seen clearly in fig. 2.6, around various k values

The analysis of the Fabry-Perot resonator is a successful model in understanding the working principles of other optical resonators. The characteristics of superpositon of fields will be helpful in analyzing the rainbow effect on chapter 4.

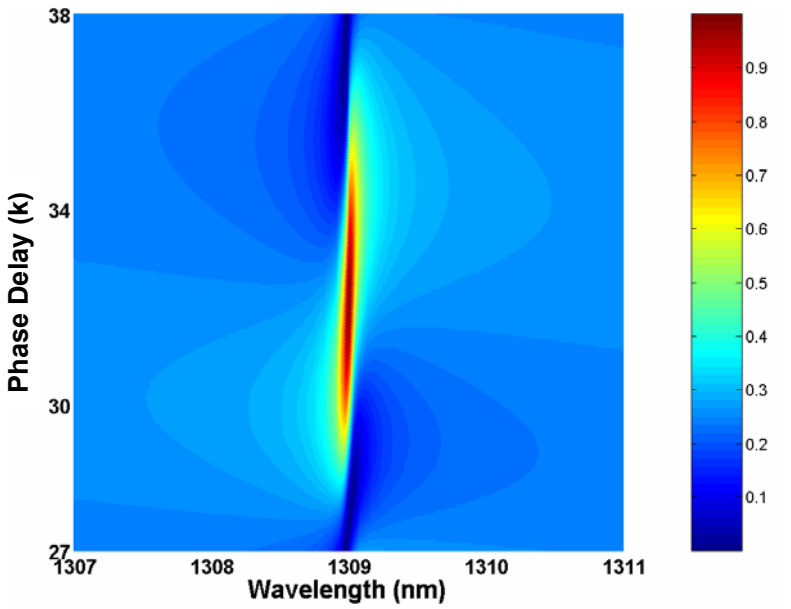

Figure 2.5. Transmission intensity for addition of two fields in a Fabry-Perot resonator.

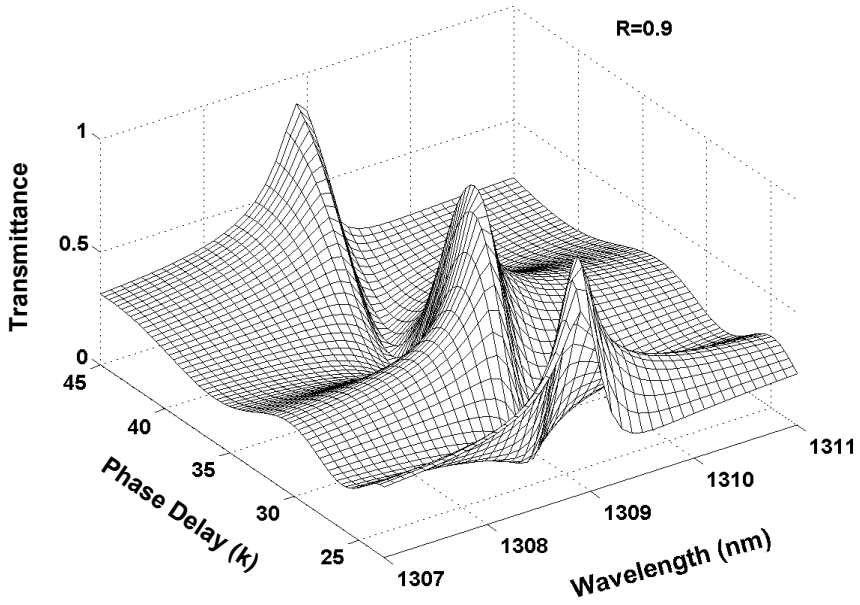

Figure 2.6. Phase-induced transmission intensity for addition of two fields in a Fabry-Perot resonator.

Chapter 3

MICROSPHERE RESONATOR

3.1 Microsphere

The modes of a spherical dielectric particle were first investigated by Gustav Mie at the beginning of the 19th century, in the context of light scattering from spherical particles. The scattering spectrum exhibited sharp features, which can be attributed to resonant circulation of optical energy within the sphere. These optical modes are confined by continuous total internal reflection at the dielectric air interface and are often referred to as 'whispering-gallery modes'. This description originated from the "problem of the whispering-gallery," which Lord Rayleigh published in 1912 [26], describing the phenomenon of acoustical waves he had observed propagating around the interior gallery of the Saint Paul's Cathedral in London, England.

The intuitive picture describing morphology dependent resonances (MDRs) is based on geometric optics picture. MDRs can be viewed as propagation of rays around the internal surface of a microsphere such that, once within the spherical particle, they are confined by total internal reflection (TIR) and repeatedly intersect beyond the critical angle. In the wave optics picture, MDRs can be considered as internal standing waves with an integer number of wavelengths circulating near the microsphere surface. The quantum mechanical interpretation is based on analysis of MDRs as shape resonance [27], in which the electromagnetic energy is temporarily trapped near the surface of the sphere in a potential well. The energy of a MDR enters and leaves the well by tunneling through the centrifugal barrier that forms the outer wall of the potential well.

The ray and wave optics description of light interaction with a microsphere has several limitations: it cannot explain escape of light from a MDR for perfect spheres. Furthermore, ray and wave optics provides no possibility for incident light to couple into a MDR, and the polarization of light is not taken into account. Finally, the radial character of the optical modes cannot be determined.

All of these issues are explained by the Maxwell wave equations with appropriate boundary conditions.

3.2. Lorenz Mie Theory

A complete description of the interaction of light with a dielectric is given by the electromagnetic theory. The spherical geometry suggests expanding the fields in terms of vector spherical harmonics. Characteristic equations for the MDRs are derived by requiring continuity of the tangential components of both the electric and magnetic fields at the boundary of the dielectric sphere and the surrounding medium. Internal intensity distributions are determined by expanding the incident wave (plane-wave or focused beam), internal field, and external field, all in terms of vector spherical harmonics and again imposing appropriate boundary conditions.

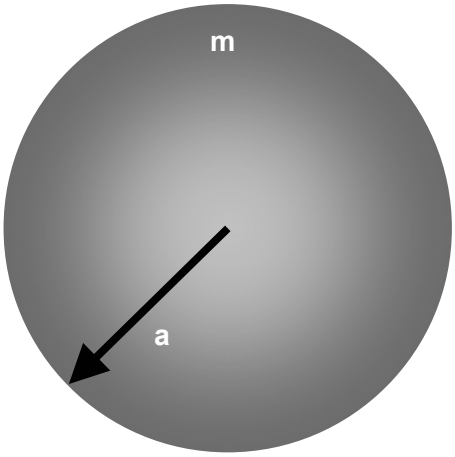

Figure 3.1. The microsphere of radius *a* and refractive index *m*.

MDRs occur at discrete wavelengths that depend sensitively on relative refractive index **m** and radius **a** of the sphere. Each MDR is labeled [28] by an azimuthal mode number (*m*), polar mode number (*n*), and a radial mode order (*l*) summarized in table 3.1, in which we prefer to use that is most common in electromagnetic-wave community rather than the notation used in quantum mechanics. The angular mode number (*n*) gives the number of azimuthal maxima in the internal intensity distribution between 0^o to 180^o. The radial mode order (*l*) indicates the number of maxima in

Parameter	Our notation (EE)	QM Notation
Refractive index	**m**(ω)	**n**(ω)
Azimuthal mode number	*m*	*m*
Polar (angular) mode number	*n*	*l*
Radial mode order	*l*	*v*

Table 3.1. Summary of Notation

the internal intensity distribution in the radial direction. For each polar mode number n, the allowed azimuthal mode numbers are in the range of −n < m < n, leading to a 2n+1degeneracy of the azimuthal modes [29].

For a perfect sphere, all of the *m* modes are degenerate (with 2*n*+1 degeneracy). The degeneracy is lifted when the cavity is axisymmetrically (along the z-axis) deformed from sphericity, shown in fig 3.1. For such distortions the integer values for *m* are ±*n,* ± (*n* − 1),...0*,* where the degeneracy remains, because the MDR's are independent of the circulation direction, i.e., clockwise or counterclockwise. Highly accurate measurements of the clockwise and counterclockwise circulating *m*-mode frequencies reveal a splitting due to internal backscattering, that couples the two counter-propagating modes.

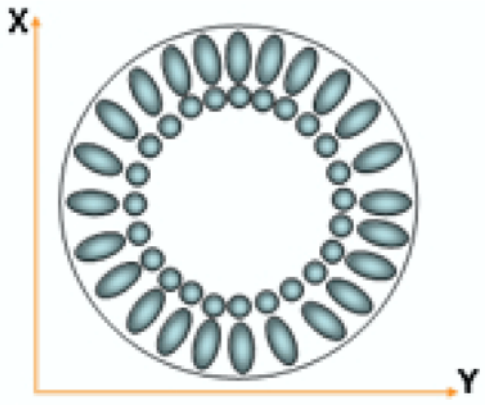

Figure 3.2. Internal-intensity distribution in the equatorial plane for a TE MDR with *n* = 12, ℓ = 2.

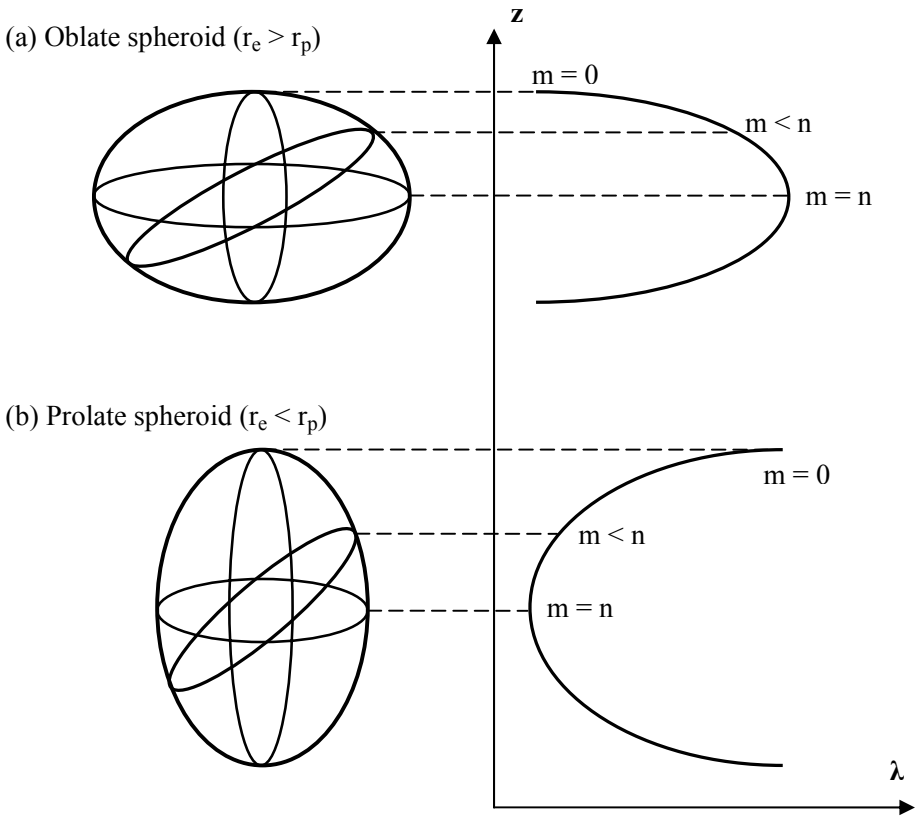

Figure 3.3. The effect of shape deformation on the emission from the various regions of sphere rim.

In addition to *n* and *l*, the resonances are characterized by their transverse magnetic (TM) and transverse electric (TE) polarization. In the standard Mie scattering formalism [30] the expansion coefficients for the scattered TM field are found by

$$a_n = \frac{j_n(x)[mxj_n(mx)]' - m^2 j_n(mx)[xj_n(x)]'}{h_n^{(2)}(x)[mxj_n(mx)]' - m^2 j_n(mx)[xh_n^{(2)}(x)]'} \tag{3.1}$$

and the coefficients for the scattered TE field are found by

$$b_n = \frac{j_n(x)[mxj_n(mx)]' - j_n(mx)[xj_n(x)]'}{h_n^{(2)}(x)[mxj_n(mx)]' - j_n(mx)[xh_n^{(2)}(x)]'} \tag{3.2}$$

where j_n is the spherical Bessel function, $h_n^{(2)}$ is the Henkel function of the second kind, and the prime indicates a derivative with respect to the argument [31]. The expansion coefficients of the internal fields of the TM (c_n) and TE (d_n) modes have the same denominators as a_n and b_n, respectively. The zeros of denominators of a_n (c_n) give the TM and b_n (d_n) correspond to TE modes of a MDR labeled by *n* and *l*, which quantizes the polar angle and radial directions [32].

3.3. Properties of MDRs

The basic properties of MDRs defining the characteristics of resonance structure are Q-factor of a MDR, mode spacing between resonances ($\Delta\lambda$), and MDR position. Q-factor describes the sharpness of a MDR, mode spacing give the distance between consecutive modes, and finally providing the position of the modes presents the full picture of a scattering intensity spectrum. For spheres with large x, several expressions are derived to determine the spectral location, separation, and width of MDRs.

3.3.1. Q-factor

The quality (Q) factor determines how long a photon can be stored inside a MDR. The Q-factor of the MDR is proportional to the ratio of the energy stored and the energy lost because of the radiation leakage during one round-trip within the microsphere. Q-factor is also defined as $Q = \omega\tau$ where ω is the optical angular frequency and τ is the radiation lifetime in the microsphere [33].

For frequencies near an MDR, the electric field inside the cavity varies as

$$E(t) = E_0 \exp(-i\omega_0 t - \frac{\omega_o}{2Q}t) \tag{3.3}$$

The decay term leads to a broadening of the resonance linewidth, giving a Lorentzian lineshape for the energy distribution

$$|E(\omega)|^2 \propto \frac{1}{(\omega-\omega_0)^2+(\omega_0/2Q)^2} \tag{3.4}$$

Alternatively, the sharpness of any resonance is commonly described by the quality factor Q. The quality Q-factor of a MDR, ($Q = \lambda/\Delta\lambda_{1/2}$), gives information about the lifetime(τ) and linewidth ($\Delta\lambda_{1/2}$) of the resonance [34]. Q-factor and wavelengths of MDRs of microspheres are highly sensitive functions of the sphere size and refractive index. For a definite MDR mode order *l*, the Q-factor of the MDR increases with increasing sphere radius; however, for a given radius **a**, the Q-factor of the MDR decreases with increasing mode order. The highest Q-factor MDRs are obtained with lower mode orders (*l*) and higher mode numbers (*n*), in which the electric field is concentrated close to the inner surface. Higher Q-factor MDRs are more sensitive to perturbations than lower Q MDRs.

3.3.2. Mode Spacing

A MDR satisfies resonance condition for specific values of the size parameter $x = 2\pi a/\lambda$, where λ is the wavelength of the incident light and **a** is the radius of the sphere. The mode spacing is defined as the wavelength difference between two consecutive mode numbers *n* in the same mode order *l*, and given by [35]

$$\Delta\lambda_{n,l} = \lambda_{n+1,l} - \lambda_{n,l} = \frac{\lambda^2}{2\pi a}\frac{\tan^{-1}(\sqrt{m^2-1})}{\sqrt{m^2-1}}, \tag{3.5}$$

for $x \approx n \gg 1$. The mode spacing is defined for TE or TM polarization and approximately same for both TE and TM modes. Comparing with the mode spacing of Fabry-Perot resonators in eq. (2.10) and that of microsphere resonators in eq. (3.5), the effective refractive index of a microsphere resonator can be defined as

$$m_{eff} = \frac{\sqrt{m^2-1}}{\tan^{-1}(\sqrt{m^2-1})} \tag{3.6}$$

which shows that as the refractive indices of the resonator approaches unity, the mode spacing of Fabry-Perot and microsphere resonators become closer as depicted in fig. 3.2.

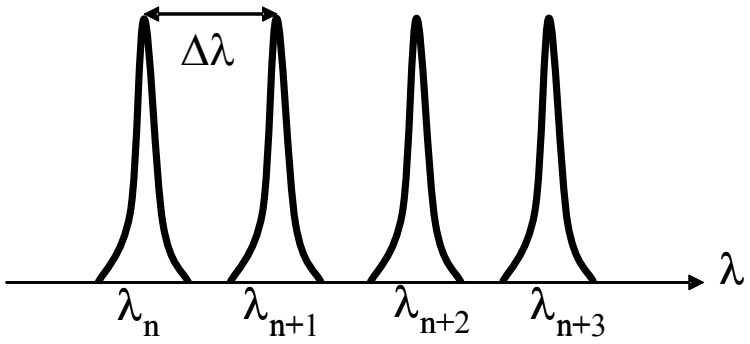

Figure 3.4. The MDRs and mode spacing Δλ between consecutive modes

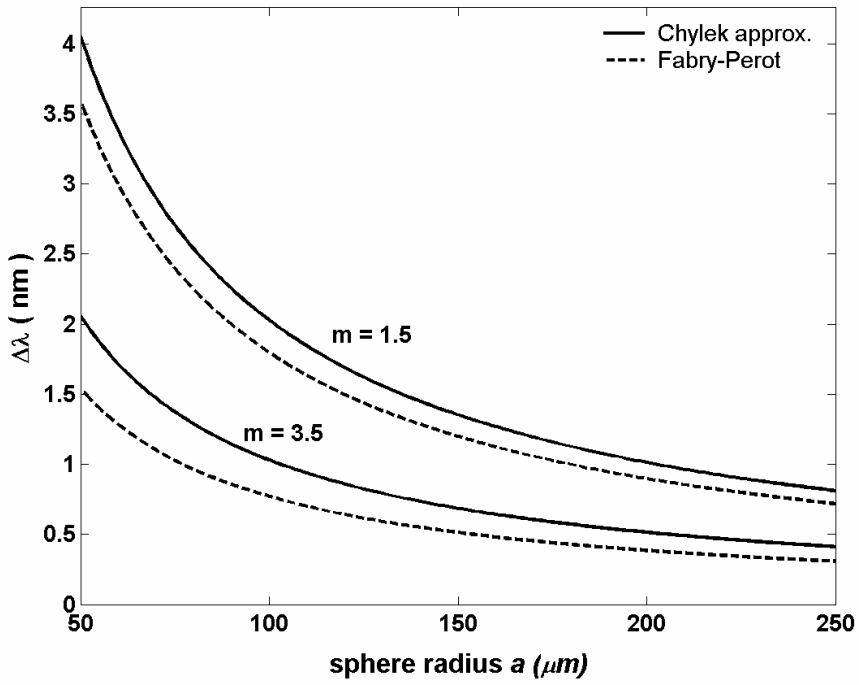

Figure 3.5. The mode spacing for Fabry-Perot and microsphere resonator with m = 1.5 and m = 3.5.

3.3.3. Mode Position

The field distribution and the resonance locations are determined by matching the solutions interior and exterior to the sphere at the dielectric-air boundary [36], leading to a characteristic equation. For a microsphere this requires matching the Bessel function $j_l(ka)$ and the outgoing Henkel functions $h_l(ka)$ at the dielectric boundary. The positions of MDR's are approximated by [37, 38]

$$mx_{n,l} = \upsilon + \alpha_l 2^{-1/3}\upsilon^{1/3} - \frac{P}{\rho} + \alpha_l^{\,2}\left(\frac{3}{10}2^{-2/3}\right)\upsilon^{-1/3} - \frac{P(m^2 - 2P^2/3)}{\rho^3}\alpha_l 2^{-1/3}\upsilon^{-2/3} + O(\upsilon^{-1}), \quad (3.7)$$

where P= m for TE modes, P=1/m for TM modes, $\upsilon = l+1/2$, $\rho^2 = m^2-1$ and α_l are the roots of the Airy function.

3.4. Excitation of MDRs

Applications of microspheres require coupling of light into the MDRs from an external light source. There are basically two methods for exciting MDRs: plane-wave and Gaussian beam illumination.

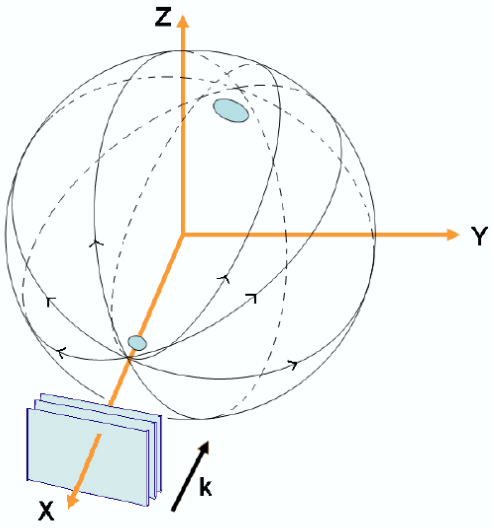

Figure 3.6. Paths of MDRs and focused spots for a plane wave illumination of microspheres.

The theoretical and experimental understanding of MDRs was extensively investigated in the case of a plane wave excitation of homogenous spherical particles [39]. In plane-wave illumination, the internal intensity is focused mostly on near the front and back surfaces of the microsphere and there is a uniform intensity distribution when the plane wave is in resonance with an MDR. However, a more efficient way to excite an MDR is to use a focused Gaussian beam aimed at the edge of a sphere [40]. The efficiency of MDR excitation for Gaussian beam illumination depends on the degree of beam focusing and the position of the beam-waist with respect to the sphere [41]. This dependence of the MDR excitation efficiency on the properties of the beam is intuitively sensible, since a large percentage of the corresponding rays in a focused beam incident somewhat beyond the particle's edge have the correct impact parameter for MDR excitation, whereas most of the rays in a loosely focused beam or a plane wave do not.

3.4.1. Gaussian Beam Excitation

The study of the fiber microsphere system depicted in Fig. 3.3 requires an extension of Lorenz-Mie theory of plane wave illumination and referred to as generalized Lorenz-Mie theory (GLMT) [42]. Gaussian beam scattering of tight beam localization was constructed and implemented a decade ago by the GLMT [43,44]. The model suitably predicts the large coupling efficiency of MDR's, when the spherical particle is illuminated near its edge by an off-axis Gaussian beam [45].

The coupling of laser light into a microsphere is crucial in efficient power transfer. Light can be coupled into the microsphere using different types of coupling devices: side-polished optical fibers [46], prisms [47], and tapered optical fibers [48]. These coupling geometries provide efficient energy transfer to the MDR through the evanescent field of the coupling device. A microsphere coupled to a fiber is depicted in Fig. 3.3. The microsphere is placed a vertical distance **b** (impact parameter), which should satisfy $b/a \leq n$ for the excitation of an MDR. Efficient coupling can be expected, if two main conditions are satisfied: phase synchronism and significant overlap of the MDR mode and the coupler mode. The coupling is based on the fact that coupler mode extends beyond the core-cladding interface [49].

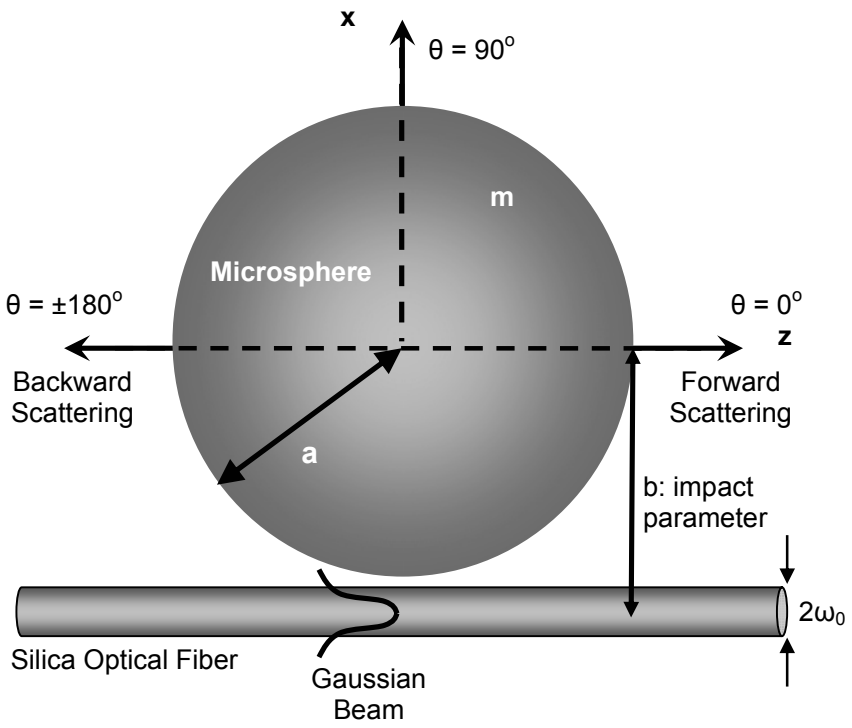

Figure 3.7. Gaussian beam excitation geometry of microspheres.

In our coupling geometry, there are four factors that influence the coupling efficiency: the fiber diameter (~$2\omega_0$), the sphere size (**a**), the fiber-sphere gap, and the ambient refractive index [50]. Larger spheres (a > 200 μm) are more suitable to attain high Q-factor MDRs but small coupling efficiencies; therefore, decreasing the microsphere size decrease Q-factor but improves the coupling efficiency and leads to larger mode spacing. Stronger coupling can be achieved by adjusting the diameter of the fiber and microsphere so that the fiber mode matches the sphere mode [51]. Immersing the microsphere in an liquid that is index matched to fiber cladding makes the optical modes less strongly confined and increases the coupling efficiency. Critical coupling is possible with proper design of the microsphere-OFHC system by optimizing sphere size, fiber diameter, the OFHC-microsphere gap.

3.4.2. Generalized Lorenz Mie Theory

The scattering theory for a spherical, isotropic, homogeneous, nonmagnetic particle illuminated by a plane wave was described by the Lorenz-Mie theory. However, it was experimentally observed that focused Gaussian beam excites the MDRs of microspheres more efficiently than plane wave. Generalized Lorenz-Mie theory (GLMT), which is a direct extension of the methodology of plane-wave Lorenz-Mie theory, describes the electromagnetic scattering of an arbitrary light beam by a spherical microparticle [52].

There are difficulties with the usual treatment of laser beams as paraxial Gaussian beams, referred to as zeroth-order Gaussian beam. First, the solution is based on a paraxial approximation to the scalar wave equation. Secondly, the distribution which approximately satisfies the wave equation is the transverse component of the electric field, but the other two components are not worked out. Therefore, higher-order corrections for the electric field of a Gaussian beam should be of use in applications where there is a need to obtain accurate solutions for the electromagnetic field of a strongly focused laser beam. The description of zeroth- and higher-order approximations to a Gaussian beam is given in appendix A.

Davis [53] presents a procedure for developing a higher-order corrected Gaussian beam description and provides expressions for the electric field components in orders of beam confinement parameter s, which is equal to the beam waist radius ω_0 divided by the diffraction length ($k\omega_0^2$), i.e.,

$$s = \frac{\omega_0}{k\omega_0^{\,2}} = \left(\frac{1}{2\pi}\right)\frac{\lambda}{\omega_0}, \tag{3.8}$$

and diffraction length is given by

$$L = \frac{\omega_0}{s} = \frac{2\pi\omega_0^{\,2}}{\lambda}, \tag{3.9}$$

where k and λ are the wave-number and wavelength of the incident beam, respectively.

Afterwards, for the scattering coefficients of spherical particle irradiated by a fifth-order Gaussian beam are presented [54] for the special case of the particle center located on the propagation axis of the beam. This description provides a significantly improved solution to Maxwell's equation as compared to first-order description, however, adds computational complexity. Also, fifth-order Gaussian beam described in this work are presented for the special case on-axis illumination of a spherical particle.

The accuracy of GLMT for an off-axis beam depends on the beam confinement parameter *s*, and it is known that first order approximation accurately describes a Gaussian beam and satisfies Maxwell's equations with a maximum error less than 1.5% for s ≤ 0.08 [55]. The procedure we followed is based on GLMT, in which the electromagnetic fields describing the incident beam is a first order approximation to an off-axis Gaussian beam [56]. The accuracy of different-order approximations is given in table A.1 of appendix A.

To mu knowledge, no work is done for the description of scattering particle irradiated by a higher-order Gaussian beam for the general case of off-axis illumination. The electric and magnetic fields of the first-order off-axis Gaussian beam propagating in medium of refractive index n, parallel to z-axis with center of the beam waist at (x_f, y_f, z_f) are given by

$$E_i = A\left(\hat{x} + \frac{2isD(x - x_f)}{\omega_0}\hat{z} \right), \tag{3.10}$$

$$B_i = A\frac{m}{c}\left(\hat{y} + \frac{2isD(y - y_f)}{\omega_0}\hat{z} \right), \tag{3.11}$$

with

$$A = E_0 \exp\left[-ik(z - z_f) \right] \times \exp\left\{ -\frac{D\left[(x - x_f)^2 + (y - y_f)^2 \right]}{{\omega_0}^2} \right\} \tag{3.12}$$

$$D = \frac{\omega_0}{\omega_0 - 2i(z - z_f)s}, \tag{3.13}$$

in rectangular coordinates. Eq 3.10 and 3.11 includes an explicit information that most efficient excitation of TE- and TM-polarized resonances depends on the beam position [57] such that eq. 3.10 is a function of x and eq. 3.11 is a function of y. TE-polarized and TM-polarized resonances are most efficiently excited when the sphere is illuminated with a beam on the x-axis and on the y-axis, respectively.

3.4.3. Excitation Efficiency of MDRs

The excitation efficiencies for the TE-polarized and TM polarized scattering, for a given partial wave (mode number) n, can be defined as the ratio of the elastically scattered power by the MDR mode divided by the incident power:

$$\sigma_{TE} = P_{scatt}^{TE} / P_i , \tag{3.14}$$

$$\sigma_{TM} = P_{scatt}^{TM} / P_i , \tag{3.15}$$

Excitation efficiency of MDRs depends on the beam waist of the Gaussian beam and the power coupled into a mode [58], which can be expressed as

$$\frac{d\varepsilon}{dt} = \langle \sigma_{\mathrm{mod}\,e} \rangle P_i - \frac{\varepsilon}{\tau}, \tag{3.16}$$

where ε is energy stored in the mode with time constant τ, $\langle \sigma_{\mathrm{mod}\,e} \rangle = \sigma_{\mathrm{mod}\,e} / \sigma_{total}$ denotes the power coupling efficiency (ratio of partial-wave scattering cross section to the total cross-section), and P_i is the incident beam power. Scattering (coupling) efficiency of a Gaussian beam can be estimated by

$$\left\langle \sigma_{\mathrm{mode}} \right\rangle_{Gaussian} = \frac{\sqrt{2}\lambda}{\pi^2 \omega_0} \tag{3.17}$$

using an intuitive ray theory. Based on Lorenz-Mie Theory, the MDR excitation efficiencies can be evaluated [59] using the relations in Appendix A. The highest-efficiency beam position is

$$b = \omega_0 s(n+\frac{1}{2}) = \frac{\lambda}{2\pi}(n+\frac{1}{2}), \tag{3.18}$$

and at the highest-efficiency beam position, the excitation efficiency is

$$\sigma_{TE} \approx \sigma_{TM} \approx \left(\frac{2}{\pi}\right)^{3/2} \frac{\lambda}{\omega_0} \approx 0.508 \frac{\lambda}{\omega_0}, \tag{3.19}$$

which shows that the maximum MDR efficiency is independent of the partial-wave number n or whether the resonance is TE or TM polarized. Eq. 3.19 concludes that when the beam waist diameter is on the order of wavelength, most of the incident beam can be coupled to MDRs of microspheres. Coupling efficiency of 99.97% is also experimentally observed with a beam waist diameter almost equal to the wavelength in a fiber-taper-coupled microsphere system [60].

Chapter 4

RAINBOW EFFECT ON RESONANCES

Rainbows have been the object of fruitful scientific research for centuries, apart from being one of the most beautiful of atmospheric phenomena [61]. The first satisfactory explanation for the existence and shape of the rainbow was given by Descartes in 1637 without a satisfactory explanation for the color formation. Thirty years later, Newton was able to account for the colors [61]. Descartes used a combination of experiment and theory to deduce that both the primary and secondary bow are caused by refraction and reflection in spherical raindrops. The light in a rainbow is often much brighter than light from nearby regions of the sky, and the physical origin of the enhancement is well understood. The scattering enhancement associated with the rainbow glory is partly caused by the spherical symmetry of the droplets, since a spherical particle exhibits a focusing effect that may occur in the forward direction [62].

4.1 Geometrical Optics

Geometrical optics contributes to the scattering from microsphere after reflections and transmissions after undergoing one or more internal reflections. Contrary to MDRs, rainbows are independent of the microsphere size and depend only on refractive index and incident angle of the ray. Ray picture of MDRs and rainbows is depicted in Fig. 4.1 showing the scattering of resonances and rainbows. A beam may be imagined as rays. A ray incident on a sphere at an angle θ_i splitted into externally reflected (p=0), and internally transmitted rays. After refraction into the sphere, the transmitted ray encounters another surface boundary and therefore is partially transmitted (p=1) and reflected, where p denotes the number of transmission on boundaries.

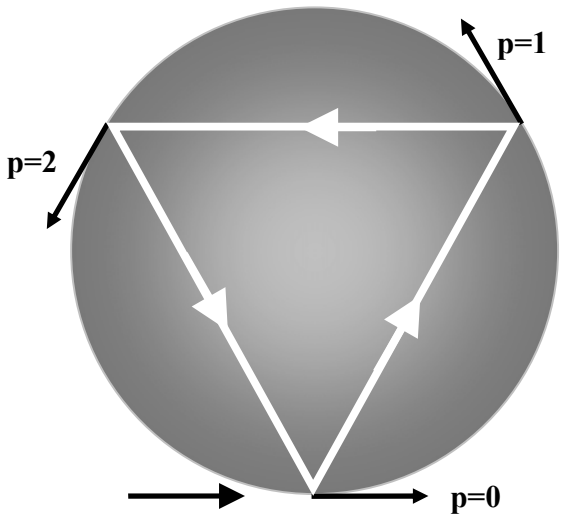

Figure 4.1. Ray representation of three periodic internal reflections.

A ray incident upon a sphere at an angle θ_i refracts to an angle θ_t satisfying Snell's law,

$$\sin\theta_i = m\sin\theta_t . \tag{4.1}$$

After p-1 internal reflection of the geometrical ray before leaving the sphere, the scattering angle corresponding to the deflection can be found by as the remainder of the rotation angle of the ray divided by 2π,

$$\theta = \mathrm{mod}\{\ [(p-1)\pi + 2\theta_i - 2p\theta_t],\ \ 2\pi\ \}, \tag{4.2}$$

which restricts the scattering angle of the ray in $-\pi \le \theta \le +\pi$, after defining $\theta > \pi$ as $2\pi-\theta$.

The position of the rainbows depends on the refractive index of the sphere and angle of incidence, and they are observed theoretically [63] and experimentally [64] in droplets. The analysis of rainbows in scattering of off-axis Gaussian beam illumination of a spherical particle is handled previously [65] by GLMT.

4.1.1. Gaussian Beam Excitation Geometry

Due to the structure of Gaussian beams, the tail of the Gaussian beam strikes the sphere with decreasing intensity and smaller angle with the normal of the sphere. A Gaussian beam incident on a sphere can be considered in ray optics as a collection of rays with maximum intensity at the center and decreasing towards its tail. The ray picture of a Gaussian beam is shown in fig. 4.1 with two representative rays incident at different angles. By using eq. (4.2), scattering angle of the tangential ray which refracts first into the sphere with $\theta_i = \pi/2$ is

$$\theta_{R1} = p(\pi - 2\theta_{t1}), \tag{4.3}$$

and scattering angle of the tail of Gaussian beam with $\theta_{i2} = \pi/2-\varphi$ is

$$\theta_{R2} = p\pi - 2\varphi - 2p\theta_{t2} \tag{4.4}$$

It follows from Snell's law (4.1) that the transmission angles determined by *m* and angle of ray with the surface normal as

$$\theta_{t1} = \sin^{-1}(1/m), \tag{4.5}$$

$$\theta_{t2} = \sin^{-1}\left[\frac{\sin(\pi/2-\varphi)}{m}\right] = \sin^{-1}\left(\frac{\cos\varphi}{m}\right). \tag{4.6}$$

Eq. (4.3) and (4.4) together with (4.5) and (4.6) can be written as a function of the angular spreading φ of the incident rays as

$$\theta_{R1} = p\pi - 2p\sin^{-1}\left(\frac{1}{m}\right), \tag{4.7}$$

$$\theta_{R2} = p\pi - 2\varphi - 2p\sin^{-1}\left(\frac{\cos\varphi}{m}\right), \tag{4.8}$$

therefore, after considering that first ray is incident on the sphere with an angle of φ behind second ray, the angular spread $\Delta\theta_R = |\theta_{R1} - \theta_{R2}|$ is read as

$$\Delta\theta_R = 2\varphi - 2p(\theta_{t1} - \theta_{t2}), \tag{4.9}$$

$$\Delta\theta_R = 2\varphi - 2p\left[\sin^{-1}\left(\frac{1}{m}\right) - \sin^{-1}\left(\frac{\cos\varphi}{m}\right)\right], \tag{4.10}$$

as a function of incident spreading of the rays, refractive index of the sphere and order *p* of the rainbow. Eq. (4.10) shows the scattering angles between θ_{R1} and $\theta_{R1}-\Delta\theta_R$ in the plane shown in fig. 4.2. Considering a Gaussian beam incidence on a sphere, effective angle of incidence φ of the tail of Gaussian beam determines the distribution of scattering pattern together with the refractive index *m* of the sphere.

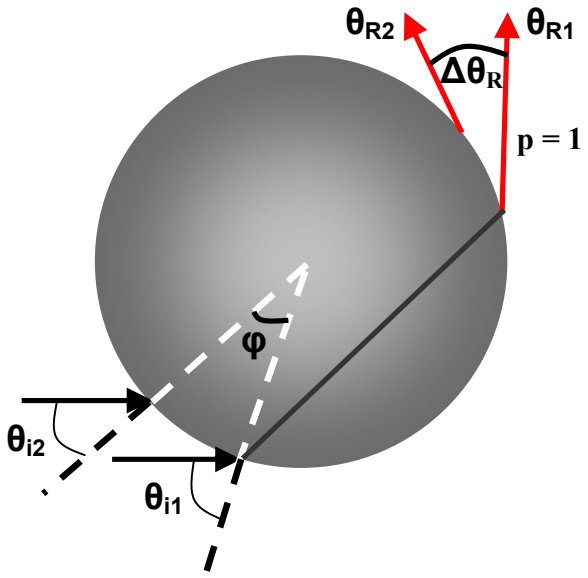

Figure 4.2. Geometrical optics picture of the incident and scattered rays.

4.1.2 Rainbow-enhanced Scattering

Scattering angle θ_R is solely determined by *m* for a tangentially incident ray, which generally results in infinite number of rainbow angles for every p. However, specific values of *m* can be determined easily to restrict the number of rainbow angles to a finite number. If a ray refracted into the sphere returns to its initial position after reflections from the surface, then a finite number of rainbows form since the ray will follow the same path in the subsequent reflections. Therefore, a finite number of rainbows will appear if reflections have a periodicity. For this type of development to be realized, at least three reflections should be included in the process, in which the number of reflections may be interpreted as the frequency (n_R) of the rainbow. The frequency of rainbows n_R=2 is physically impossible, because refraction of a tangential ray parallel to the normal of the surface requires the refractive index to be infinite. The minimum possible value for rainbow frequency (number of rainbow angles) is $n_R = 3$. The first four promising rainbow geometries are depicted in fig. 3 for n_R = 3, 4, 5, and 6. For a tangentially incident ray, it follows from eq. (4.5) that the periodic rainbows form when the integer multiple of refraction angle is equal to 2π. By using eq. (4.5), the scattering angle of the tangential ray can be found as

$$\theta_{R1} = \frac{2p\pi}{n_R}, \qquad p \le n_R, \tag{4.11}$$

for a periodic rainbow picture of the p^{th} order rainbow with frequency $n_R \geq 3$. The periodic rainbow structure restricts the refractive index of the sphere to discrete values

$$m = \frac{1}{\sin\left(\frac{\pi}{2}\frac{(n_R - 2)}{n_R}\right)}, \qquad n_R = 3,4,5,\ldots, \tag{4.12}$$

which gives m as a function of rainbow frequency. Increasing the period of the rainbows leads to a lower refractive index *m* as shown in fig 4. Minimum frequency of n_R = 3 gives the maximum possible value of refractive index *m* = 2.

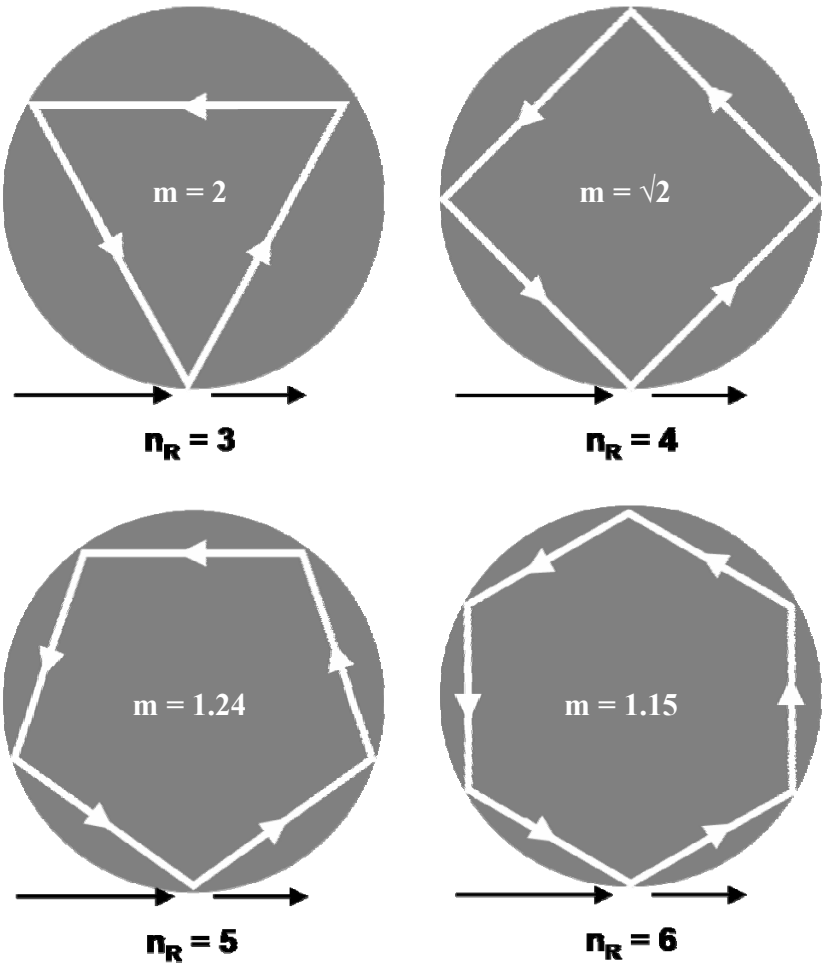

Figure 4.3. Periodic rainbow formation geometries for $n_R = 3$, 4, 5, and 6 for edge excitation.

The next order refractive indices are $m = \sqrt{2}$ and 1.236 for $n_R = 4$ and 5, respectively. As the rainbow frequency increases, the corresponding refractive index decreases almost exponentially and approaches its limit of $m = 1$ for frequent rainbows. As the frequency of the rainbows increases or refractive index decreases, the scattering angle of the tangential ray becomes smaller and rainbows become closer. However, because of the spreading of rainbow found in eq. (4.10), rainbow angles may not be distinguished clearly, depending on the incidence angle of the incoming beam.

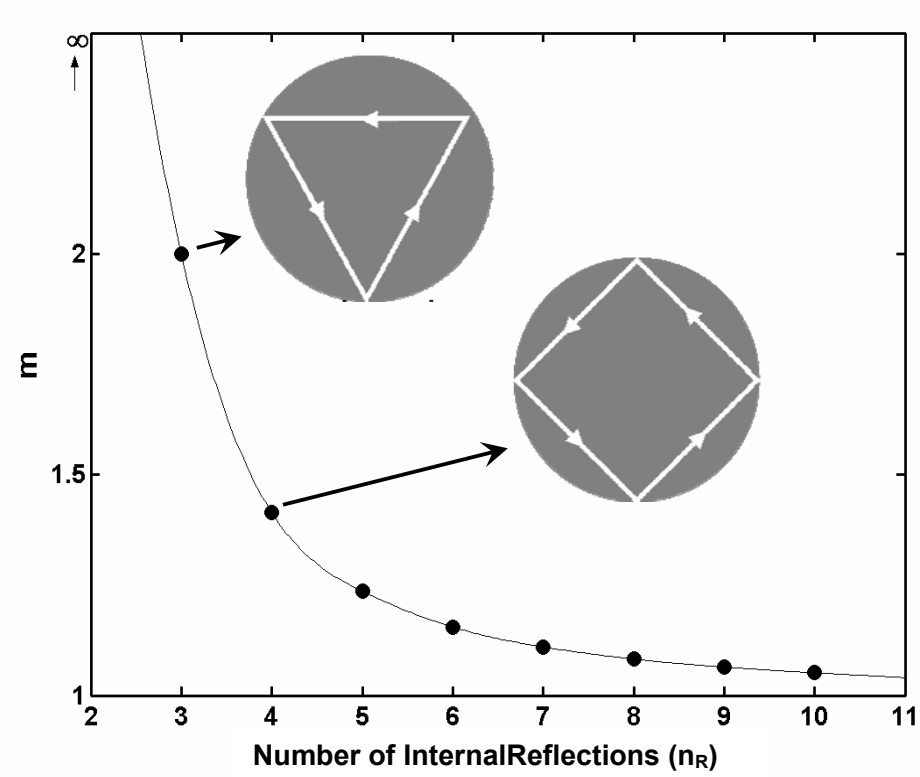

Figure 4.4. Refractive index (m) of a sphere as a function of periodic rainbow reflections (n_R).

4.2. Scattered Field Intensity

The internal field intensity of a microsphere at a particular location or angle in xz plane of fig. 4.2 is given by $\mathbf{E}\cdot\mathbf{E}^*$, where $\mathbf{E}$ is the electric field amplitude. Electric field amplitude at a given angle can be decomposed into electric field amplitude of a MDR (M) and background (B). They can be written at a given polar angle (θ) as

$$E_M(\theta) = E_{M_0} \exp\left(i\vec{k}_M \cdot \vec{r} - \omega t\right), \tag{4.13}$$

$$E_B(\theta) = E_{B_0} \exp\left(i\vec{k}_B \cdot \vec{r} - \omega t\right), \tag{4.14}$$

where k_M and k_B represent the wave number of MDR and background electric field, respectively. Fig. 4.5 shows the constant background electric field amplitude and MDR fields with Lorentzian line shapes around resonance wavelengths.

By the superposition of fields, scattered electric field amplitude is given by

$$E_s(\theta) = E_M(\theta) + E_B(\theta), \tag{4.15}$$

which leads to a total scattered electric field intensity,

$$I_s(\theta) = E(\theta) \cdot E^*(\theta) \tag{4.16}$$

$$I_s(\theta) = \left| \vec{E}_M(\theta) + \vec{E}_B(\theta) \right|^2. \tag{4.17}$$

Therefore, scattering intensity is found to be,

$$I_s = E_{M_0} E_{M_0}{}^* + E_{B_0} E_{B_0}{}^* + 2E_{M_0} E_{B_0}{}^* \exp(i\Delta\vec{k} \cdot \vec{r}), \tag{4.18}$$

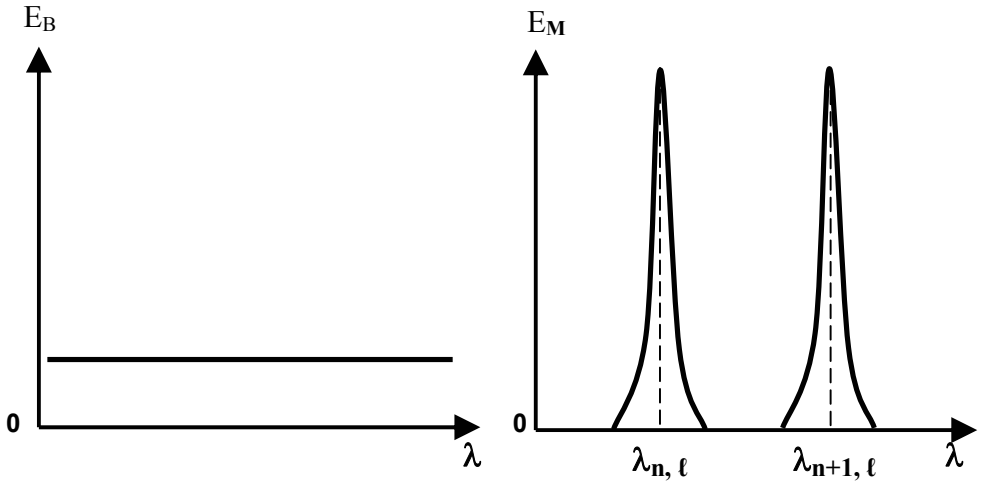

Figure 4.5. Electric field of the background (rainbow) field (E_B) and MDR field (E_M).

or in a more compact form

$$I_s = I_M + I_B + 2E_{M_0}E_{B_0}{}^{*}\exp(i\Delta\vec{k}\cdot\vec{r}), \tag{4.19}$$

where its k-vector is

$$\Delta\vec{k} = \vec{k}_M - \vec{k}_B, \tag{4.20}$$

and phase of the intensity can be defined as

$$\phi = \Delta\vec{k}\cdot\vec{r} \tag{4.21}$$

where $\vec{k}_M$ is uniform and $\vec{k}_B$ depends on rainbow angles which give rise to phase dependence of the total intensity in eq. (4.19). Therefore, we expect to observe in phase and out-of-phase crossings at MDRs around rainbow angles as depicted in fig. 4.6.

Although background field does not contribute to an MDR, they are active as a ray and contribute to the rainbow formation by refraction. Therefore, rainbow angles are expected to reveal phase-dependent behavior in scattering. Therefore, there will be three possible intensity behaviors in the scattering intensity around rainbow angles, shown in fig. 4.6.

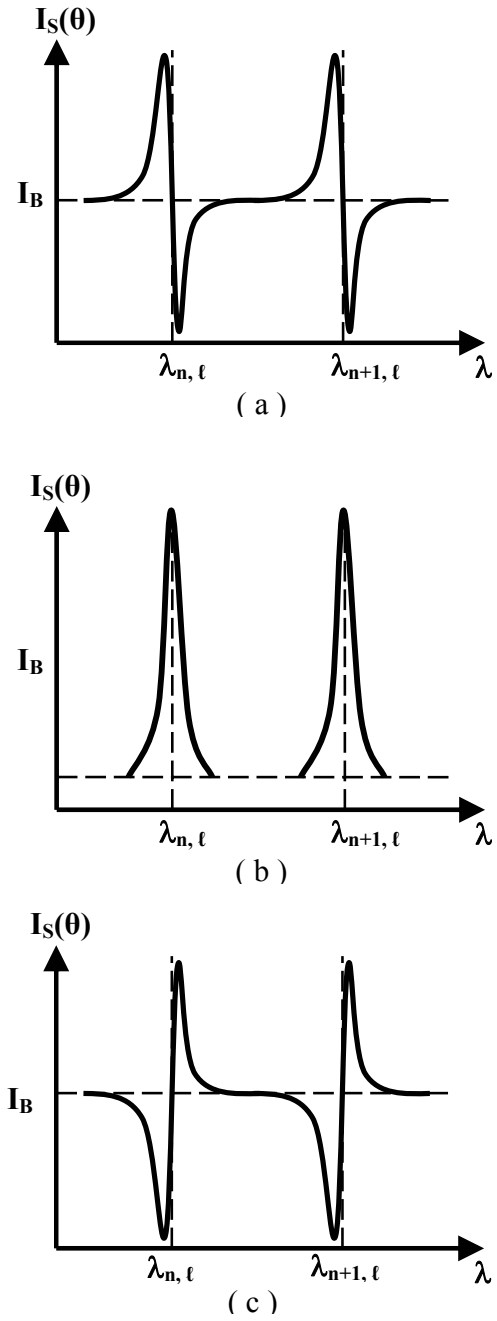

Figure 4.6. Superposition of rainbow (E_B) and MDR field (E_M) results in three possible phase-induced scattering intensity.

4.2.1. Rainbow Enhanced Scattering

In this section, calculations based on GLMT are presented assuming focused-beam illumination, instead of plane-wave, illumination of a microsphere to explore the effects of superposition of rainbows and MDRs in the scattering intensity spectra. A fundamental Gaussian beam propagating in the z axis direction with a beam-waist radius of w_0 is modeled with a first-order corrected Gaussian-beam to determine the electromagnetic field components of the incident beam. The model used in the calculations is accurate for $s \leq 0.1$ so that $\lambda/\omega_0 \leq 0.63$.

The model used in the calculations is based on the geometry shown in fig. 3.3. The Gaussian beam is guided through a silica fiber to excite the MDRs of the microsphere. As an example, we studied the angularly resolved scattering intensity of a microsphere of a = 10 μm and refractive index m = 2.0 excited with a Gaussian beam. Illuminating beam has a beam waist of ω_0 = 1.75 μm in the wavelength region λ = 1300 - 1330 nm and is propagating at an impact parameter b = 11.75 μm from a microsphere. The size parameter of the microsphere is x = 70 and the beam has a beam confinement factor of s = 0.08. The scattered intensity is calculated in the whole x-z plane.

The expected spectrum of the angularly resolved scattering intensity is illustrated in fig. 4.7, for a sphere of refractive index $m = 2$. The special refractive index $m = 2$ lets only three rainbows to appear in the scattering spectrum as studied in section 3. The corresponding angle of rainbows is found from eq. 4.12 that they occur around 120^o, -120^o, and 0^o with a finite angular spreading. The rainbow angles are represented by three horizontal rows in fig. 4.7. The resonance wavelengths are determined by the radius and refractive index of the sphere; however, the rainbow angles are determined only by the refractive index of the sphere. Three vertical lines in the spectrum arise at the MDR positions and they are sharper than the rainbows; therefore, the superposition of rainbows and MDRs leads to bright patterns directed along the MDRs. The intensity of rainbow-enhanced resonances is distinguishably high around rainbow angles. High Q-factor resonances lead to wavelength-dominated scattering intensity. However, as the Q-factor of resonances decreases, the scattered field intensity becomes angle-dominated and spreads in rainbow angles.

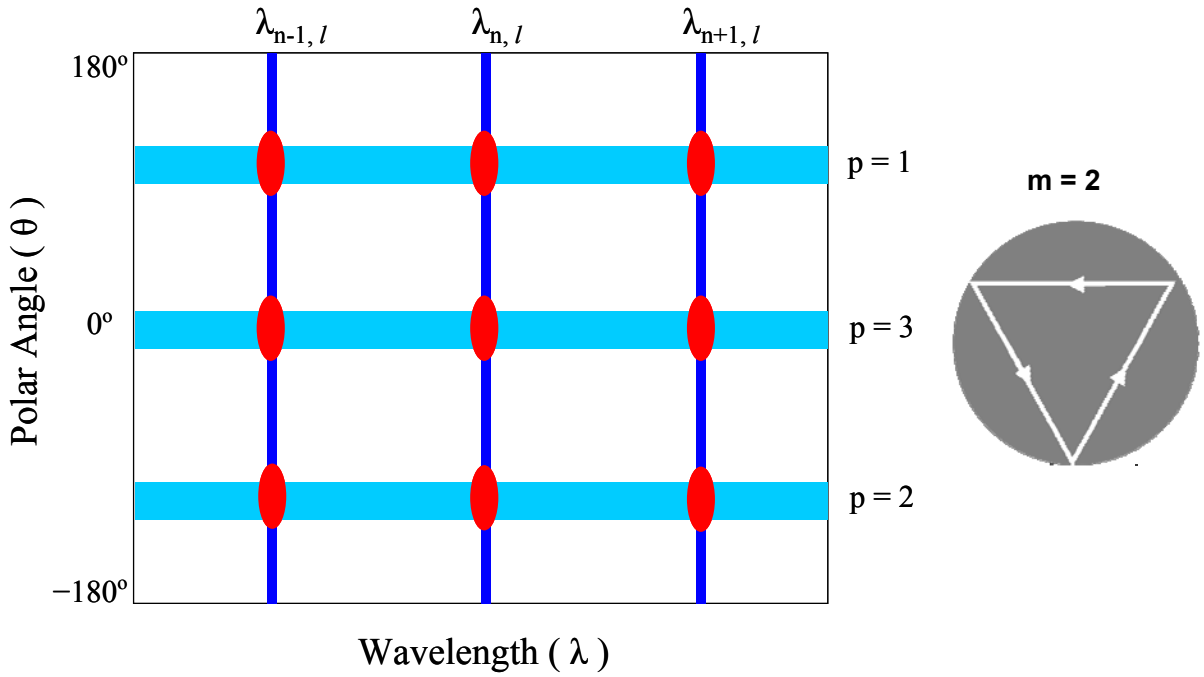

Figure 4.7. Expected spectra for the superposition of rainbows and MDRs for a sphere with m = 2 (three horizontal bars show the three possible rainbow angles around $\theta = \pm 120^{o}$ and 0^{o}).

In the analysis of rainbow-enhanced resonances, we studied TE and TM scattering intensity spectra in the wavelength region of 1300-1330 nm. Fig. 4.8 shows the angularly resolved scattering intensity pattern for the TE component of the scattered field and TM component of the scattered field is shown in fig. 4.10. The calculations are performed using sampling resolution of λ_{res} = 5 pm and θ_{res} = 1^{o}. The zoomed images, 4.9 (a-b) and 4.11 (a-b), of a small part of the scattered field reveals greater detail about the rainbow enhanced MDRs. The sampling resolution for the zoomed images are λ_{res} = 1 pm and θ_{res} = 0.2^{o}. The highest observable MDR has Q-factor of 10^{6}. The rainbow in the forward direction is mostly masked by uncoupled part of the incident beam as observed in fig. 4.8 and 4.10.

4.2.2. TE component

There are three observable modes in the wavelength region with mode spacing $\Delta\lambda \approx 11.5$ nm. The twin and wider MDRs are closer to each other and located at (1301.72 nm, 1301.95 nm), (1313.12 nm, 1313.51 nm), and (1324.49 nm, 1324.81 nm) with Q-factors about 10^{4}. The sharper MDRs are at

1303.87, 1314.86, and 1326.04 nm with Q-factors about $5x10^5$. The observable spreading for the first order rainbow is between 75° and 125°, skewed towards lower angles, with the highest intensity around 105° which deviates from 120° since rainbow forms as a cooperative effect of incident rays components of the Gaussian beam. The second order rainbow appears between −100° and −150°, skewed towards lower angles.

Fig. 4.9 (a, b) show higher resolution image of the portions framed in fig. 4.8. There two modes in the wavelength region of 1302.5 – 1304.5 nm, with Q-factor = 10^4. The MDR wavelengths are 1313.12 nm and 1313.51 nm. The Q-factor of MDR at 1313.12 nm is 10 times lower than that of the MDR at 1313.51 nm; therefore, while lower Q-factor MDR is skewed along the rainbow angle, higher Q-factor MDR is directed along the resonance wavelength. The scattering intensity is concentrated on the rainbow and there is no observable intensity carried on the MDR relative to the rainbow part. For a higher Q-factor MDR shown in fig 4.9 b, the MDR wavelength is at 1314.86 nm. The Q-factor = $5x10^5$ causes the intensity to be directed along the resonance wavelength.

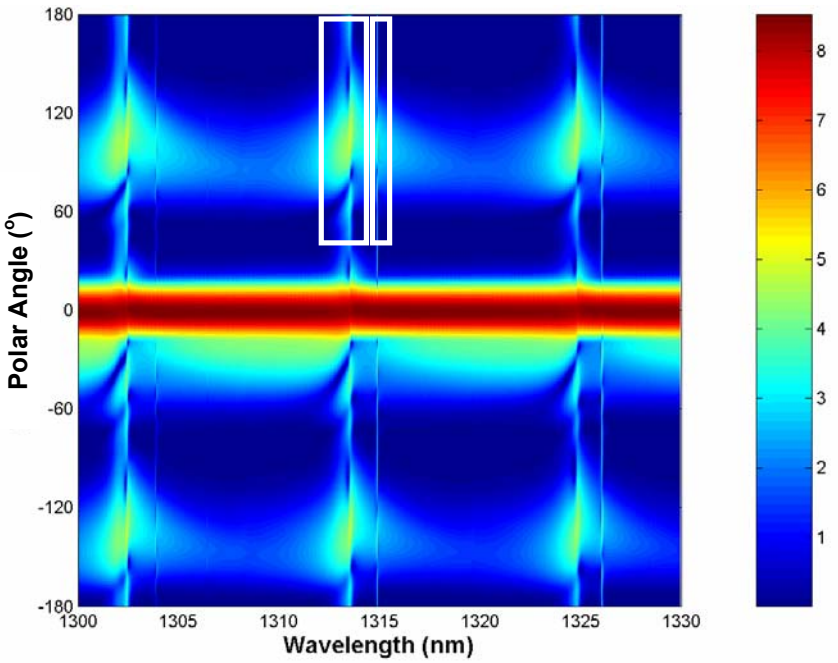

Figure 4.8. Low resolution color image of the intensity of transverse electric (TE) elastic light scattering from a microsphere with a radius of 10.00 μm and refractive index of m=2.

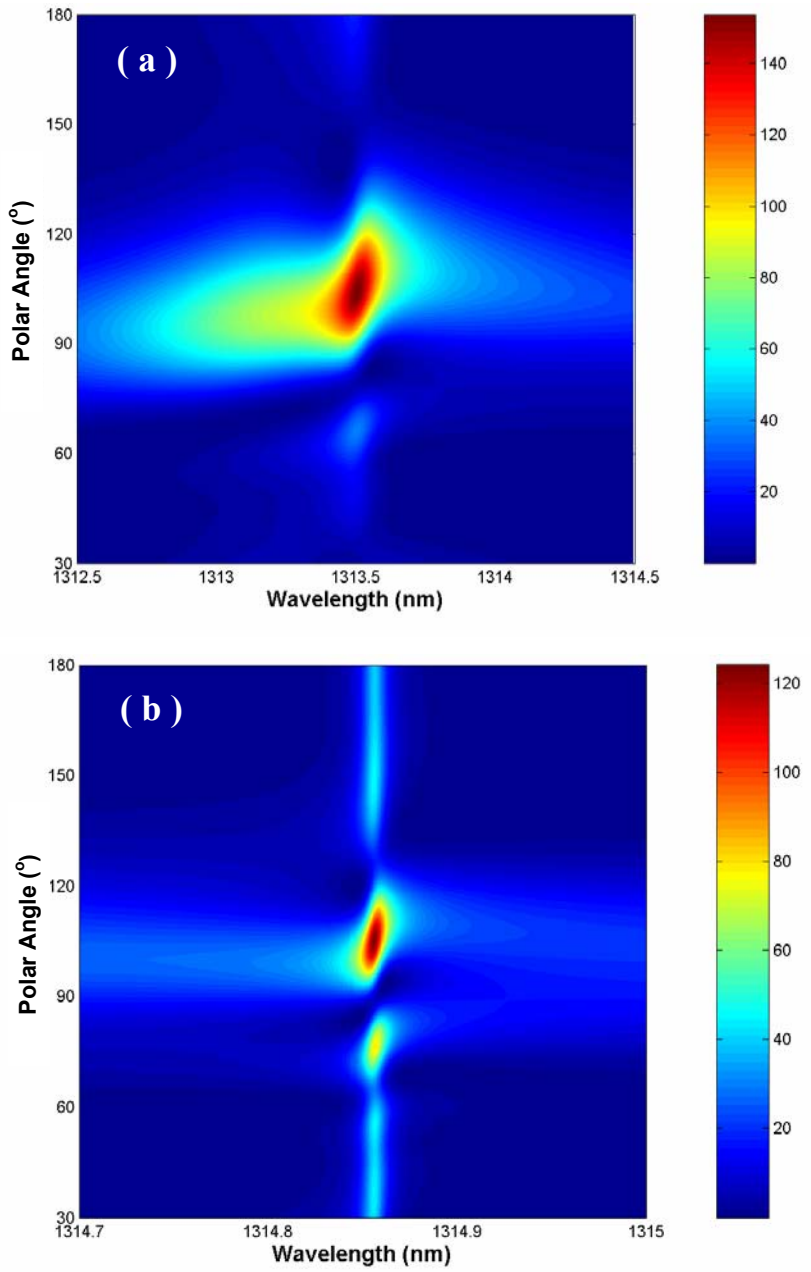

Figure 4.9. High resolution color image of the TE light scattering intensity with wavelength resolution of 0.001 nm and angle resolution of 0.2°. The spectra shows (a) Angle-oriented scattering intensity for a low Q-factor MDR (b) Wavelength-oriented scattering intensity for a high Q-factor MDR.

4.2.3. TM component

There are two observable modes in the wavelength region with mode spacing $\Delta\lambda \approx 11.5$ nm. The twin and wider MDRs are closer to each other and located at (1308.15 nm, 1308.4 nm) and (1319.53 nm, 1319.60 nm) with Q-factors about 10^4. The sharper MDRs are at 1310.26 and 1321.30, and with Q-factors about $5\text{x}10^5$. The observable spreading for the first order rainbow is between 85^o and 125^o, skewed towards lower angles, with the highest intensity around 120^o which deviates from 120^o since rainbow forms as a cooperative effect of incident rays components of the Gaussian beam. The second order rainbow appears between -100^o and -150^o, skewed towards lower angles.

Fig. 4.11 (a, b) show higher resolution image of the portions framed in fig. 4.10. There are two modes in fig. 4.11(a) in the wavelength region of 1318.5 – 1320.5 nm, with Q-factor = 10^4. The MDR wavelengths are 1319.53 nm and 1319.60 nm. The Q-factor of MDR at 1319.53 nm is 10 times lower than that of the MDR at 1319.61 nm; therefore, while lower Q-factor MDR is skewed along the rainbow angle, higher Q-factor MDR is directed along the resonance wavelength. The scattering intensity is concentrated on the rainbow and there is no observable intensity carried on the MDR relative to the rainbow part. For a higher Q-factor MDR shown in fig 4.11(b), the MDR wavelength is at 1321.30 nm. The Q-factor = $5\text{x}10^5$ causes the intensity to be directed along the resonance wavelength.

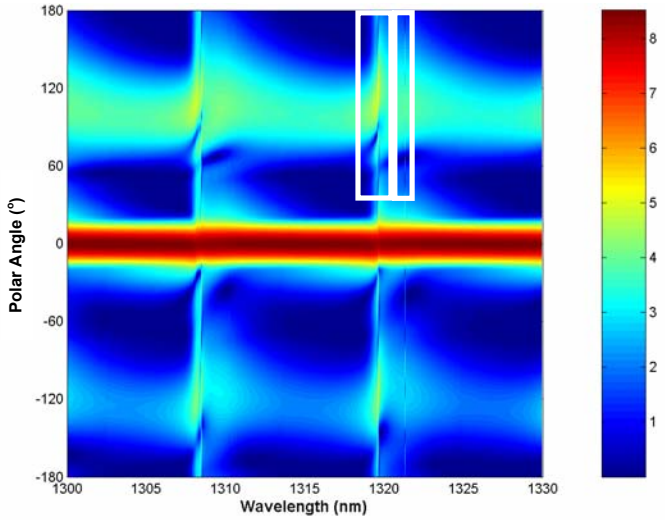

Figure 4.10. Low resolution color image of the intensity of transverse magnetic (TM) elastic light scattering from a microsphere with a radius of 10.00 μm and refractive index of m=2.

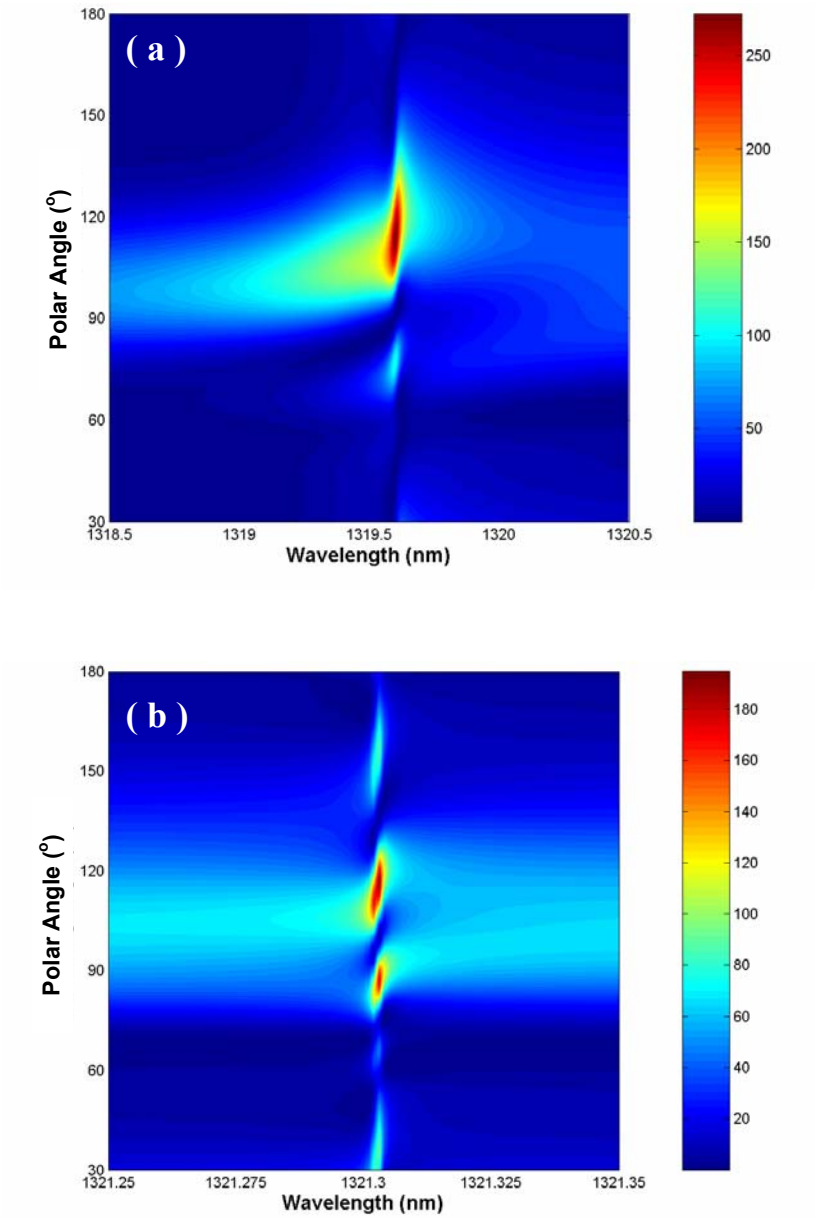

Figure 4.11. High resolution color image of the TM light scattering intensity with wavelength resolution of 0.001 nm and angle resolution of 0.2^{o} (a) Angle-oriented scattering intensity for a low Q-factor MDR (b) Wavelength-oriented scattering intensity for a high Q-factor MDR.

4.2.4. Phase Effect on MDRs

As studied in the beginning of the section, $\vec{k}_M$ is uniform and $\vec{k}_B$ depends on rainbow angles which give rise to sensitivity around rainbow angles due to phase dependence of the total intensity in eq. (5.7). Therefore, we expect to observe in phase and out-of-phase crossings at MDRs around rainbow angles as depicted in fig. 4.6.

The TE scattering intensity for the intersection of MDR wavelength and 1st order rainbow is shown in fig. 4.12, for m = 2 in the polar angle between 60-150°. The mesh curve shows the scattering intensity with a wavelength resolution of λ_{res} = 2 pm and angle step of θ_{res} = 5°. The effective region of rainbow spreading is in the scattering angle region of 105±15°. The phase-induced scattering depicted in fig. 4.6 is realized in the angularly resolved scattering intensity spectra. Rainbow-enhanced scattering is observed with maximum intensity in the vicinity of 105° (depicted in fig. 4.6b). Before observing maximum intensity, phase-induced intensity of fig. 4.6a is observed in the region of 90-100°. After the maximum intensity, phase-induced intensity depicted in fig. 4.6c is observed in the region of 110-120°.

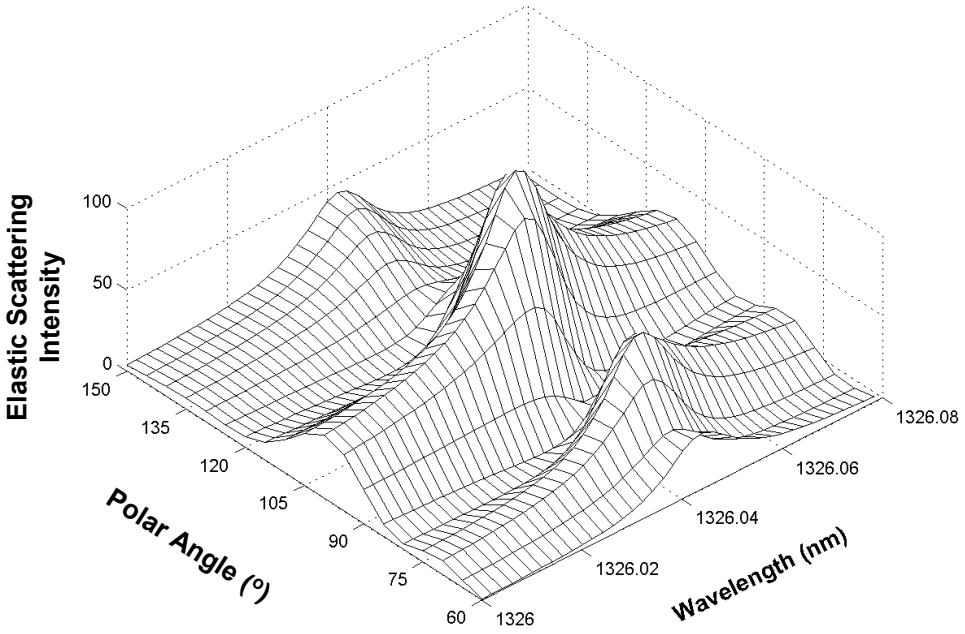

Figure 4.12. Phase-induced TE scattering intensity for a MDR around 1st order rainbow.

The TM scattering intensity for the intersection of MDR wavelength and 1st order rainbow is shown in fig. 4.13, for m = 2 in the polar angle between 60-180°. The mesh curve shows the scattering intensity with a wavelength resolution of $\Delta\lambda$ = 3pm and angle step of $\Delta\theta = 5^{o}$. The effective region of rainbow spreading is in the scattering angle region of 105±20°. The phase-induced scattering depicted in fig. 4.6 is realized in the angularly resolved scattering intensity spectra. Rainbow-enhanced scattering is observed with maximum intensity in the vicinity of 120° (depicted in fig. 4.6b). Before observing maximum intensity, phase-induced intensity of fig. 4.6a is observed in the region of 95-110°. After the maximum intensity, phase-induced intensity depicted in fig. 4.6c is observed in the region of 115-125°.

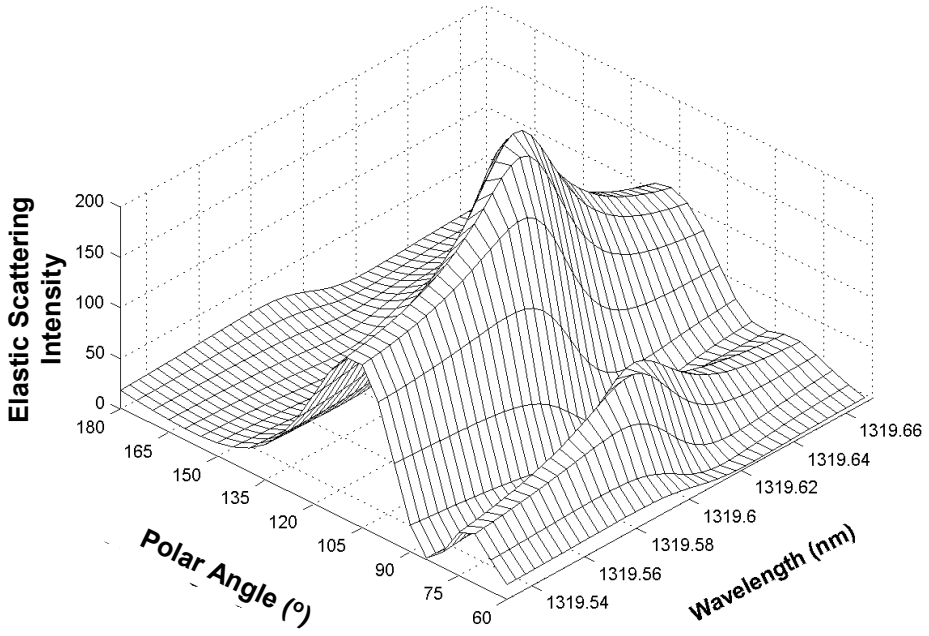

Figure 4.13. Phase-induced TM scattering intensity for a MDR around 1st order rainbow.

Chapter 5

APPLICATIONS OF MICROSPHERES

5.1. Biomolecular Detection Applications

The field of optical biosensors is rapidly evolving due to the need to overcome the limitations of the amount of material to be detected [66]. An optical biosensor detects interactions between target biomolecules in solution and probe molecules immobilized to a surface. The Fabry-Perot resonator can be used in biodetection applications [67], as shown in fig 5.1. The biomolecules attached to the surface of a plate leads to a decrease in the distance between the plates; therefore, a smaller wavelength will satisfy the resonance condition and the intensity maxima will shift to a different resonance wavelength.

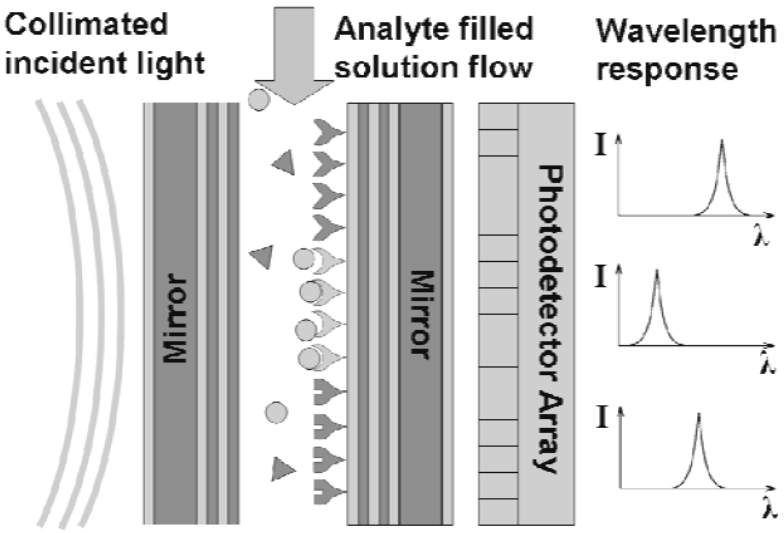

Figure. 5.1. Biomolecular detection by Fabry-Perot resonator [67].

Optical microsphere resonators with high Q-factor MDR's can be used as sensitive biodetectors. These extraordinary Q-factors, reported as large as $2x10^{10}$, translate directly to high energy density and narrow resonant-wavelength lines [68]. The sharp optical resonance of microsphere provides exceptional resolving power, down to submonolayer molecular adsorbate level. By affixing the appropriate proteins and DNA molecules to the surface of the microsphere, and measuring the Q-factor and observed shift in the resonant peak locations, the biomolecules sticking to the surface can be characterized [69]. A biomolecule such as a protein that resides in the evanescent field of MDR's can absorb light, thus influencing the MDR's [70]. The shift of MDR's by protein adsorption onto microspheres is demonstrated and modeled as a first order perturbation [71]. Recently, red shift of resonance wavelengths is used for high sensitivity label-free DNA quantification [72].

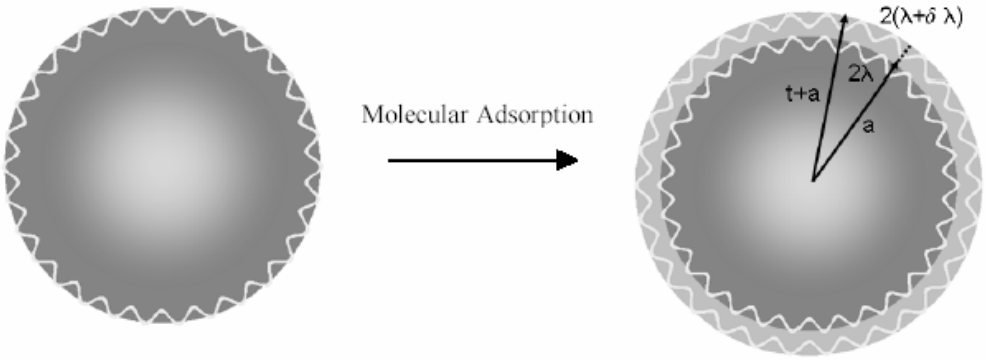

Figure 5.2. Scheme of the molecular adsorption on microsphere surface [70].

5.1.1. Perturbation Approach

A perturbation approach is applied to resonance modes in a spherical microcavity with reflective interior surface. Formulas were obtained for the frequency shift caused by a spatial change in the refractive index within the cavity [73]. A more rigorous perturbation theory was presented by Lai *et. al*. [70] to treat the effect of isotropic and anisotropic deformations of the microsphere surface on the resonance frequency shift without changing the refractive index in the exterior or in the interior of the microsphere.

The aforementioned formulations, however, do not allow one to evaluate the frequency shift that is due to changes in the medium surrounding the microsphere. Arnold *et. al.* [74] derived formulas for frequency shifts that are due to these changes. The change can be either within the sphere or in the surrounding medium. They applied these formulas to uniform refractive-index changes in the surround, to the adsorption layer, and to the refractive index profile near the surface.

To evaluate the shift $\delta\omega$ in angular frequency ω of a single protein molecule, it is useful to consider the energy interaction as a first order perturbation to a single photon resonant state, with a semiclassical field $\mathbf{E}_0(\mathbf{r})\, e^{(i\omega t)}$. The evanescent tail of the field induces dipole moment in the protein in excess of the displaced water, $\delta\mathbf{p}\, e^{(i\omega t)}$, causing a shift in the photon energy of the resonant state, $\hbar\delta\omega = -\delta\mathbf{p} \cdot \mathbf{E}_0^*(\mathbf{r}_i)/2$. The excess dipole moment can be represented in terms of the real part of an excess polarizability α_{ex}, i.e., $\delta\mathbf{p} = \alpha_{ex}\mathbf{E}_0(\mathbf{r}_i)$. The excess polarizability α_{ex} of a molecule forming the layer is its polarizability in excess of the polarizability of an equal amount of water. The fractional frequency shift for a protein positioned at $\mathbf{r}_i$ is given by the result of dividing the perturbation by the energy of the mode (i.e., $\hbar\omega$), as represented by integrating over the energy density in the interior [73]:

$$\left(\frac{\delta\omega}{\omega}\right)_i \cong \frac{-\alpha_{ex}\left|\mathbf{E}_0(\mathbf{r}_i)^2\right|}{2\int \varepsilon_s \left|\mathbf{E}_0(\mathbf{r})^2\right| dV} \tag{5.1}$$

where ε_s is the homogeneous permittivity of the microsphere. It should be noted that for protein molecules, which are composed of variety of aminoacids, α_{ex} is roughly proportional to the mass of the molecule [75], and the shift in frequency in accordance with eq. (5.1) should behave in the same way [76]. Eq. (5.1) represents the shift that is due to an individual molecule at an arbitrary position on the microsphere. For a large number of protein molecules distributed over random locations on the sphere surface, singular contribution in eq. (5.1) is summed up over randomly located molecules into a continuous sum. As a result the fractional frequency shift is given by [73]:

$$\frac{\delta\omega}{\omega} \cong -\frac{\alpha_{ex}\sigma_p}{\varepsilon_0\left(m_s^2 - m_m^2\right)a} \tag{5.2}$$

where a is the radius of the microsphere, σ_p is the protein surface density, m_s and m_m are the refractive indices of the microsphere, and the aqueous medium, respectively. Protein surface density σ_p is the number of molecules per surface area, which is calculated as layer thickness divided by molecular volume. The frequency in the Eq. (5.2) can be replaced by the wavelength (λ) and have the form :

$$\frac{\delta\lambda}{\lambda} = \frac{\alpha_{ex}\sigma_p}{\varepsilon_0\left(m_s^2 - m_m^2\right)a} \tag{5.3}$$

This equation predicts the wavelength shift for a compact molecular monolayer surface density σ_p. The equation is exact if the layer is considerably thinner than the evanescent field depth [73]. The conservation of optical size predicts a MDR wavelength shift $\delta\lambda$ as a function of the change of effective sphere radius δa as :

$$\frac{\delta\lambda}{\lambda} = \frac{\delta a}{a}. \tag{5.4}$$

5.1.2. Numerical Results

The work on this section is published in [9]. Elastic light scattering calculations are based on the geometry shown in Fig. 5.3. A silica microsphere (with refractive index of 1.5) surrounded with water (with refractive index of 1.33) is placed on an optical fiber half coupler (OFHC), and the 90° scattered and transmitted signals can be detected. A tunable laser can be used to excite the MDR's of the silica microsphere [77].

For the calculations, the beam in the OFHC is simulated by a Gaussian beam (with an infinite skirt length and a beam waist with a half-width of 1.5 μm) propagating just at the edge of a silica microsphere. The calculation is performed for a scattering angles of 90^o and 0^o (forward scattering or transmission). Fig. 5.3. shows the expected spectra in the scattering calculations.

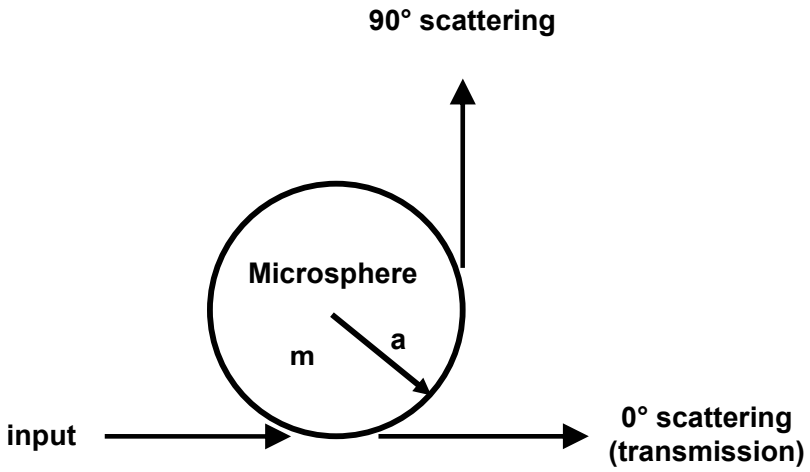

Fig. 5.3. Elastic light scattering geometry from a microsphere for biomolecular detection.

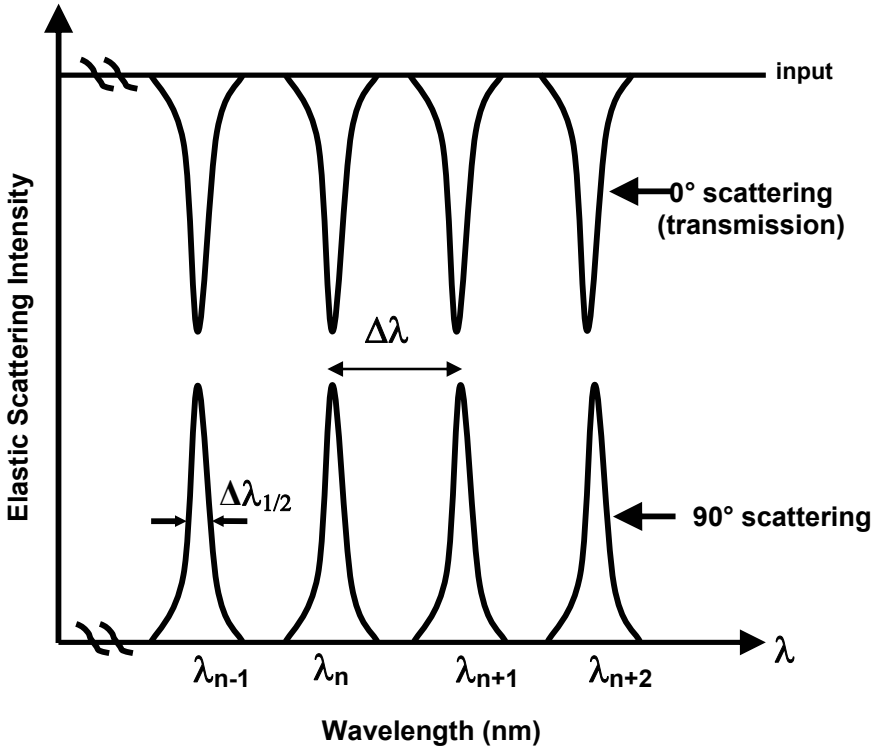

Fig. 5.4. Expected elastic light scattering in the 0° (transmission) and the 90° spectra for the configuration in fig. 5.2.

The TE and TM polarized elastic scattering spectra calculations are performed for a silica microsphere with a refractive index of 1.5, in the wavelength range of 1530 – 1560 nm and with a resolution of 0.01 nm. The radius of the microsphere is taken as 20.00 μm (coated only with the capture layer) and 20.01 μm (coated with the capture layer and the biomolecule of interest) to investigate the influence of size change in the elastic scattering spectrum. The increase in the size represents affixing of the biomolecule of interest, e.g., protein or DNA molecules. From a geometric optics point of view, enlarging the radius of microsphere will result in increasing the optical path of waves inside the microsphere; therefore, resonance condition will be satisfied at longer wavelengths, which will cause a red shift of the elastic scattering spectrum.

Fig. 5.5(a) shows the transverse electric (TE) elastic scattering spectra in the wavelength region between 1530 nm and 1560 nm for the 20.00 μm and 20.01 μm silica microspheres. The upper curves show the elastic scattering calculated for the 0° (forward scattering or transmission) angle. The lower curves show the elastic scattering calculated for the 90° angle. The mode spacing 9.5 nm correlates well with the size of the 20.00 μm silica microsphere.

Fig. 5.5(b) shows the high resolution TE elastic scattering spectra in the wavelength range of 1548.4 – 1549.6 nm with a resolution of 0.001 nm. The linewidth of resonances is around 0.01 nm leading to a quality factor ($Q = \lambda/\Delta\lambda_{1/2}$) of 10^5. The increase of 10 nm in the radius of microsphere causes a shift of 0.775 nm in the scattering spectra. The mode shift of 0.775 nm (0.05%) correlates well with the size shift of the 0.01 μm (0.05%) of the silica microsphere. The observed shift is around hundred times the resonance linewidth showing promise in identification of biomolecules. If there is less coverage of the biomolecule of interest (e.g., a typical 10% coverage), the relative shift will be 10% of the expected shift, which is still one order of magnitude bigger than the resonance linewidth.

Fig. 5.6(a) shows the transverse magnetic (TM) elastic scattering spectra in the wavelength region between 1530 nm and 1560 nm for the same 20.00 μm and the 20.01 μm silica microspheres. The upper curves show the elastic scattering calculated for the 0° (forward scattering or transmission) angle. The lower curves show the elastic scattering calculated for the 90° angle. The mode spacing 9.5 nm correlates well with the size of the 20.00 μm silica microsphere.

Fig. 5.6(b) shows the high resolution TM elastic scattering spectra in the wavelength range of 1544.0 – 1545.5 nm with a resolution of 0.001 nm. The linewidth of resonances is around 0.01 nm

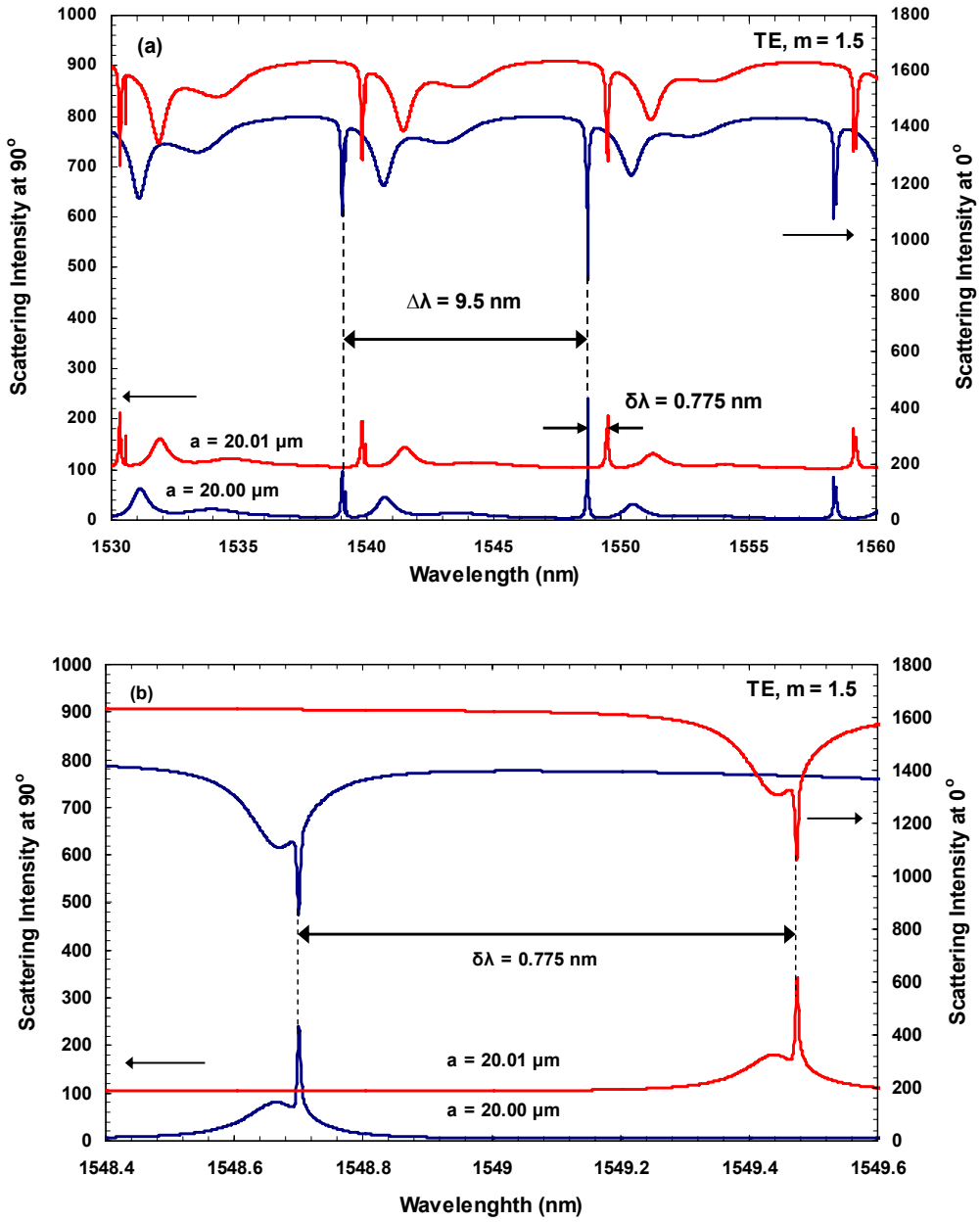

Figure 5.5. (a) Transverse electric (TE) elastic light scattering spectra from a silica microsphere with a radius of 20.00 μm and 20.01 μm. (b) High resolution TE elastic light scattering spectra from a silica microsphere with a radius of 20.00 μm and 20.01 μm.

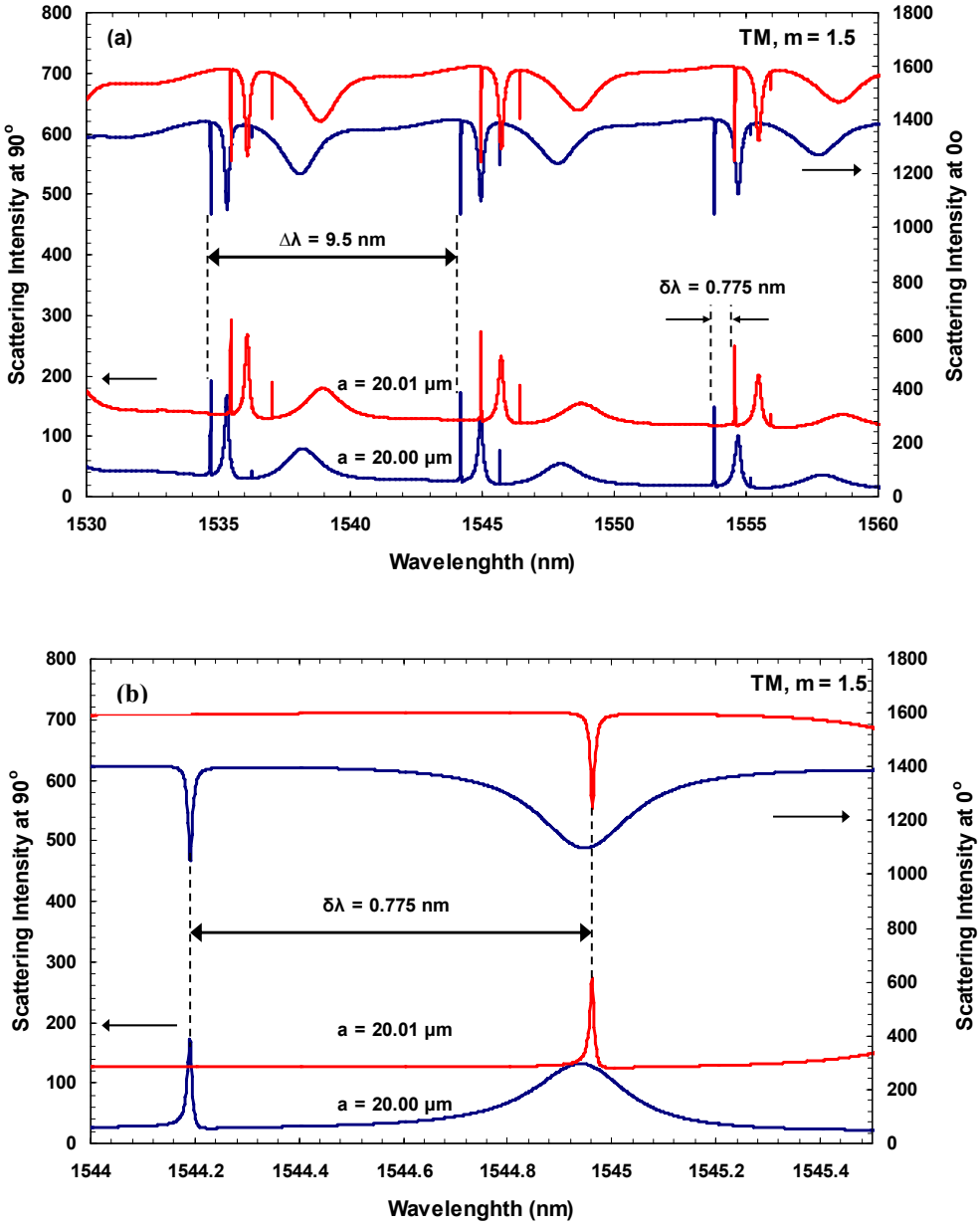

Figure 5.6. (a) Transverse magnetic (TM) elastic light scattering spectra from a silica microsphere with a radius of 20.00 μm and 20.01 μm. (b) High resolution TM elastic light scattering spectra from a silica microsphere with a radius of 20.00 μm and 20.01 μm.

leading to a quality factor ($Q = \lambda/\Delta\lambda_{1/2}$) of 10^5. The increase of 10 nm in the radius of microsphere causes a shift of 0.775 nm in the scattering spectra. The mode shift of 0.775 nm (0.05%) correlates well with the size shift of the 0.01 μm (0.05%) of the silica microsphere. The observed shift is around hundred times the resonance linewidth showing promise in identification of biomolecules. If there is less coverage of the biomolecule of interest (e.g., a typical 10% coverage), the relative shift will be 10% of the expected shift, which is still one order of magnitude bigger than the resonance linewidth.

In order to consider the concise effect of non-uniformities in the microsphere structure, the theory should be reformulated in terms of Green's functions and their renormalizations [78]. In the presence of a random perturbation, one sees that narrow resonances broaden, split, and disappear; however, wider ones are less affected and only broaden.

Furthermore, the sensitivity of MDRs to refractive index and size changes can be extended further by an accurate determination of the refractive index variation associated with phase changes around rainbow resonances. Any effect as a result of attaching a biomolecular agent can be enhanced further around rainbow angles. Therefore, the rainbow-enhanced MDRs and associated phase effects, studied in chapter 4, provide an additional tool for realization of refractive index changes and its effects on sharp MDRs of microspheres in sensing applications.

5.2. Infrared Light Scattering

In this section, the scattering of light in infra-red region of the spectrum from the microspheres will be studied. The excitation geometry is the same given in fig. 5.3 and 5.4.

In the calculations, the input light is a CO_2 laser beam with a beam waist radius of 25 μm and wavelength around 10.6 μm. An ordinary CO_2 laser has its peak power in this wavelength region used in the calculations. The laser is incident on a micrsphere of radius 250 μm with impact parameter of 280 μm. There are two observable modes in the calculations both for TE- and TM-polarized scattered light. The mode spacing between the modes is around 7 μm.

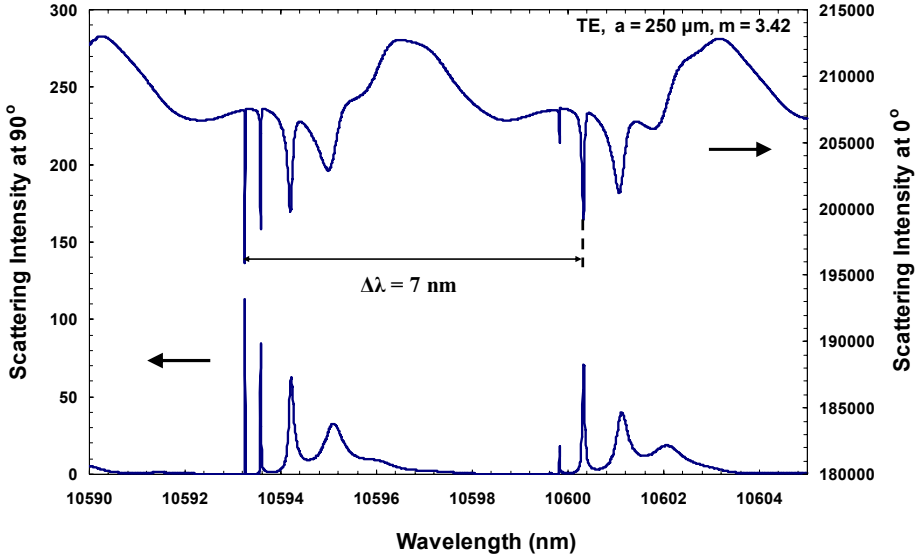

Figure 5.7. Transverse electric (TE) elastic light scattering spectra of CO_2 laser beam from a silicon microsphere with a radius of 250 μm.

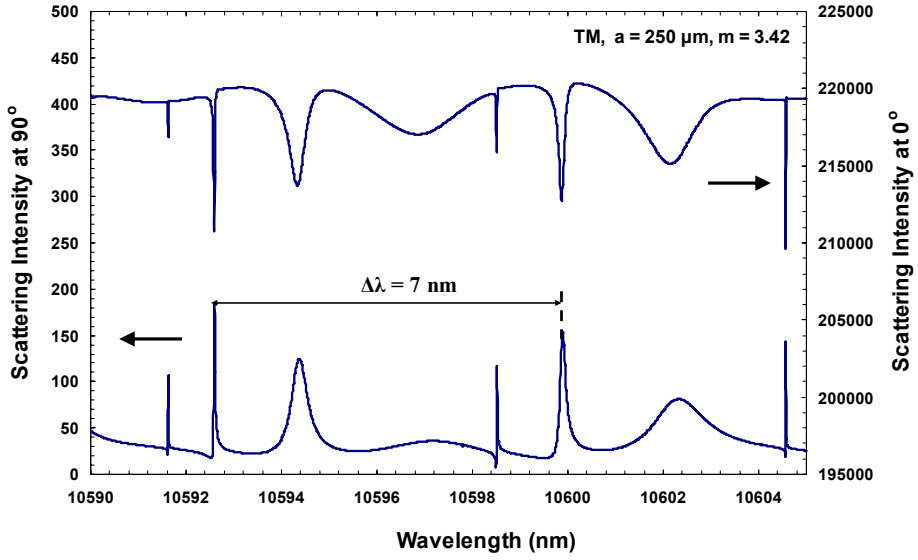

Figure 5.8. Transverse magnetic (TM) elastic light scattering spectra of CO_2 laser beam from a silicon microsphere with a radius of 250 μm.

The TE and TM polarized elastic scattering spectra calculations are performed for a silicon microsphere with a refractive index of 3.42, in the wavelength range of 10590 – 10605 nm and with a resolution of 0.01 nm. The radius of the microsphere is taken as 250 μm to investigate the scattering in the far infra-red region.

Fig. 5.7 shows the transverse electric (TE) elastic scattering spectra in the wavelength region between 10590 nm and 10605 nm for the 250 μm silicon microspheres. The upper curves show the elastic scattering calculated for the 0° (forward scattering or transmission) angle. The lower curves show the elastic scattering calculated for the 90° angle. The mode spacing 7 nm correlates well with the size of the 250 μm silicon microsphere. The linewidth of highest Q-factor resonances is around 0.01 nm leading to a quality factor ($Q = \lambda/\Delta\lambda_{1/2}$) of 10^5.

Fig. 5.8 shows the transverse magnetic (TM) elastic scattering spectra in the wavelength region between 10590 nm and 10605 nm for the 250 μm silicon microspheres. The upper curves show the elastic scattering calculated for the 0° (forward scattering or transmission) angle. The lower curves show the elastic scattering calculated for the 90° angle. The mode spacing 7 nm correlates well with the size of the 250 μm silicon microsphere. The linewidth of highest Q-factor resonances is around 0.01 nm leading to a quality factor ($Q = \lambda/\Delta\lambda_{1/2}$) of 10^5.

Chapter 6

CONCLUSION

In this work, the Fabry-Perot resonator is analyzed to recognize various effects that are observed in the elastic scattering intensity spectrum of a microsphere resonator. The rainbow formation and its consequences on MDRs of microspheres are understood based on the analysis of addition of fields in a Fabry-Perot resonator. The results showed that the Fabry-Perot resonator is a helpful model in identifying the behavior of the interference of rainbows and MDRs. The rainbow-enhanced MDRs and associated phase effects can be used in sensing as an additional tool to the refractive index and size of the microsphere that are used in traditional detection applications.

Also, elastic scattering calculations from microspheres are carried out for a silica microsphere. Silica with a refractive index of 1.5, which is very close to that of bimolecular agents, is a suitable photonic material to use for biosensing applications. The calculations showed that microsphere is a suitable candidate to be used in biomolecular detection applications.

Elastic light scattering calculations from a silicon microsphere with refractive index 3.42 were performed for optoelectronic channel dropping applications in the far infrared.

As future work, the rainbow enhanced MDRs can be examined to understand the consequences of refractive index and size changes of microspheres. In addition, the phase-induced intensities is promising for channel dropping applications since the intensity around rainbow angles fades away entirely in the spectrum at certain angles.

APPENDIX A

Gaussian Beam Description

Gaussian beam descriptions use electromagnetic field components satisfying Maxwell's equations. In geometrical optics, a straight line represents the propagation direction of the wavefront. If the lightwave is indeed a plane wave, both the **E** and **H** fields have to extend to infinity, or if the lightwave is a spherical wave, its wavefront diverges in all directions. These mathematical expressions, although adequate approximations in many situations, are not physically realizable. The Gaussian beam is a more realistic approximation from the viewpoints of both wave and ray optics. The energy of the Gaussian beam is confined within the vicinity of a straight line. The wavefront of the Gaussian beam is unique in that it behaves like a plane wave in the vicinity of the beam waist, but it gradually converts into a spherical wave as the distance from the waist increases. The beam energy, however, is always confined within a finite divergence angle. Description of Gaussian beams in paraxial (zeroth-order) limit is a well established theory [79]. Let the vector potential for a Gaussian beam be

$$u = \psi(x, y, z)e^{ikz} \tag{A. 1}$$

The amplitude function $\psi(x, y, z)$ can be a complex function. The Gaussian beam has to satisfy the wave equation

$$\nabla^2 u + k^2 u = 0\,. \tag{A.2}$$

By inserting Eq. (A.1) into (A.2), $\psi(x, y, z)$ has to satisfy

$$\frac{\partial^2 \psi}{\partial x^2} + \frac{\partial^2 \psi}{\partial y^2} + 2ik\frac{\partial \psi}{\partial z} = 0 \tag{A.3}$$

where the variation of the amplitude function ψ with respect to z was assumed to be slow, and

$$\frac{\partial^2 \psi}{\partial x^2} = 0\,. \tag{A.4}$$

Then ψ can be obtained by solving Eq. (A.3). The function

$$\psi = A\exp\left\{i\left[P(z) + k(x^2 + y^2)/2q(z)\right]\right\} \tag{A.5}$$

can be tried as a solution of eq. (A.3). The factor *A* is assumed to be constant. This solution is called the fundamental mode. The solutions, where A is a function of x and y, are called higher order modes. The quantity q(z) is a complex number referred to as the q-parameter. The q-parameter controls both the phase and the amplitude distribution in the transversal plane, and it plays an important role in describing the type of field. Insertion of Eq. (A.5) into (A.3) gives

$$2k\left(\frac{i}{q} - \frac{\partial P}{\partial z}\right) + \left(\frac{k}{q}\right)^2\left(\frac{\partial q}{\partial z} - 1\right)(x^2 + y^2) = 0 \tag{A.6}$$

an then *u* is obtained as

$$u = A\exp(\underbrace{iP(z)}_{Correction} + \underbrace{ikz + ik(x^2 + y^2)/2R(z)}_{Parabolicphase} + \underbrace{k(x^2 + y^2)/2Q(z)}_{Amplitude}\,. \tag{A.7}$$

After some manipulations, the expression for the amplitude of the Gaussian beam is rewritten as

$$u(z) = \underbrace{A}_{Cons\tan t} \underbrace{\frac{\omega_0}{\omega(z)}}_{Contaraction\ ratio} \underbrace{\exp(-iQ + ik(z + r^2/2R(z))}_{Spherical\ waveform} - \underbrace{r^2/\omega^2(z)}_{Transverse\ amplitude\ distribution} \tag{A.8}$$

where

$$r^2 = x^2 + y^2 \tag{A.9}$$

identify the transverse amplitude distribution.

$$z_0 = \frac{k}{2}\omega_0^2 . \tag{A.10}$$

is known as the Rayleigh range.

$$\omega^2(z) = \omega_0^2\left[1 + \left(\frac{z}{z_0}\right)^2\right] \tag{A.11}$$

is a measure of the beam, where ω_0 is the beam waist radius.

$$R(z) = z\left[1 + \left(\frac{z_0}{z}\right)^2\right] \tag{A.12}$$

measure the wavefront radius of curvature.

$$\phi(z) = \tan^{-1}\left(\frac{2z}{k\omega_0^2}\right) \tag{A.13}$$

is a correction factor to R(z).

The first factor in eq. (A.8) is the amplitude and the second factor is the change in amplitude due to the change in the radius of the beam. The third factor is the phasefront, which approaches that of a plane wave at the waist as well as in the far field. For intermediate distances, the phasefront approaches a spherical wavefront with radius of curvature R(z), but with a correction factor of ϕ. The last factor represents a bell-shaped transverse field distribution. From eq. (A.8), we see that only three parameters are needed to specify the Gaussian beam: the size of the beam waist, the distance from the beam waist, and the wavelength of the light.

The intensity distribution I(r, z) is given by uu^* and from Eq. (A.8) it is

$$I(r,z) = I_0\left(\frac{\omega_0}{\omega(z)}\right)^2 e^{-2r^2}/\omega^2(z) \tag{A.14}$$

The transverse distribution at a particular value of z is Gaussian. The longitudinal distribution I(0, z) along the beam axis has its maximum at the waist and decays monotonically as $[\omega_0/\omega(z)]^2$. The intensity distribution of the Gaussian beam is symmetric with respect to the waist. As soon as the distribution of I(r, z) on one side of the waist is known, that on the other side is obtained by the mirror image.

Equation (A.11) can be rewritten as

$$\left(\frac{\omega(z)}{\omega_0}\right)^2 - \frac{z^2}{z_0^2} = 1 \tag{A.15}$$

Thus, the beam radius of the Gaussian beam is a hyperbolic function of z. The beam expansion at a far distance is

$$\lim \tan\theta = \frac{2}{k\omega_0} \tag{A.16}$$

The spread is inversely proportional to the size of the waist ω_o. This is similar to the spread of the far-field diffraction pattern of a plane wave through an aperture with radius ω_0.

Higher-order Approximations to Gaussian Beam

Similar to the well-established paraxial (zeroth-order) Gaussian beam solution, the spatial coordinates transverse to the direction of propagation are normalized relative to the beam waist radius,

$$\xi = \frac{x}{\omega_0} \quad \text{and} \quad \eta = \frac{y}{\omega_0} \tag{A.17}$$

and the spatial coordinate in the direction of propagation is normalized relative to the diffraction length

$$\zeta = \frac{x}{k\omega_0^{\,2}} \tag{A.18}$$

With this change of spatial variables, the expression for the vector potential becomes

$$u = \psi(\xi, \eta, \zeta) e^{-i\zeta / s^2} \tag{A.19}$$

and Helmholtz equation, in terms of ψ, can be rearranged as

$$\left(\frac{\partial^2}{\partial \xi^2} + \frac{\partial^2}{\partial \eta^2} - 2i \frac{\partial^2}{\partial \zeta} \right) \psi = -s^2 \frac{\partial^2 \psi}{\partial \zeta^2} \tag{A.20}$$

If the beam confinement parameter s, defined in eq. (A.15), is assumed small ($\omega_0 \geq \lambda$), then from eq. (A.20), ψ can be expanded as a sum of even powers of s so that,

$$\psi = \psi_0 + s^2 \psi_2 + s^4 \psi_4 + \ldots \tag{A.21}$$

Using

$$u \approx \left(\psi_0 + s^2\psi_2 + s^4\psi_4\right)e^{-i\zeta/s^2}\hat{x}, \tag{A.22}$$

with Maxwell's equations, will give expressions for electromagnetic field components to fifth order in the parameter s.

Accuracy of Gaussian Beam Approximations

The accuracy of the approximation to an incident beam depends on a dimensionless beam confinement parameter. Higher order approximations for the electromagnetic field components of a Gaussian beam should be applied when large beam confinement parameters are used [80].

s=		0.02	0.05	0.10	0.20	0.30	0.40
s^0	avg% max%	0.817 3.07	2.10 7.94	4.37 16.8	9.47 37.0	15.3 60.8	21.8 88.0
s^1	avg% max%	1.73×10^{-2} 9.28×10^{-2}	0.111 0.603	0.457 2.51	1.90 10.3	4.33 22.6	7.74 38.4
s^2	avg% max%	6.43×10^{-4} 8.23×10^{-3}	1.05×10^{-2} 0.133	8.85×10^{-2} 1.14	0.757 10.7	2.56 31.9	5.89 49.3
s^3	avg% max%	2.36×10^{-5} 1.97×10^{-4}	9.58×10^{-4} 8.26×10^{-3}	1.61×10^{-2} 0.144	0.2777 2.51	1.44 19.1	4.25 36.0
s^4	avg% max%	1.15×10^{-6} 2.46×10^{-5}	1.19×10^{-4} 2.52×10^{-3}	4.10×10^{-3} 8.85×10^{-2}	0.148 3.99	1.13 38.2	3.85 54.0
s^5	avg% max%	5.13×10^{-8} 7.58×10^{-7}	1.27×10^{-5} 1.99×10^{-4}	8.69×10^{-4} 1.40×10^{-2}	6.19×10^{-2} 1.19	0.725 22.2	3.34 3.36

Table A.1. Average and maximum percent error of the Maxwell's equations for zeroth- to fifth-order Gaussian beam description.

Table A.1 provides a comparison of the percent error for s=0.02, 0.05, 0.10, 0.20, 0.30 and 0.40 for zeroth- to fifth-order Gaussian beam descriptions.

Generalized Lorenz-Mie Theory

Based on Lorenz-Mie Theory, the MDR excitation efficiencies can be evaluated [81] using the relations:

$$\sigma_n^{TE} = 8(n+\frac{1}{2})s^2 \exp\left\{-2\left[\frac{b^2}{\omega_0^2}+s^2\left(n+\frac{1}{2}\right)^2\right]\right\}\times\left[I_0(2Q_{o.c.})-\cos 2\phi_0 I_2(2Q_{o.c.})\right], \quad \text{(A.23)}$$

$$\sigma_n^{TM} = 8(n+\frac{1}{2})s^2 \exp\left\{-2\left[\frac{b^2}{\omega_0^2}+s^2\left(L+\frac{1}{2}\right)^2\right]\right\}\times\left[I_0(2Q_{o.c.})-\cos 2\phi_0 I_2(2Q_{o.c.})\right], \quad \text{(A.24)}$$

for both arbitrary ω_0 and arbitrary transverse positioning of the beam waist center (x_0, y_0, 0). I_0 and I_2 are the modified Bessel functions. The arguments in eq. (A.23, A.24) are

$$b = \sqrt{x_0^{\,2}+y_0^{\,2}} \quad \text{(A.25)}$$

$$Q_{o.c.} = 2s\left(n+\frac{1}{2}\right)b/\omega_0 \quad \text{(A.26)}$$

where $Q_{o.c.}$ is called the off-centeredness of the beam with a partial wave *n*. If the beam strikes the spherical particle far off-axis with b ≈ *a*, then $Q_{o.c}$ is large and the excitation efficiencies can be approximated by

$$\sigma_n^{TE} = \frac{4s^2(n+\frac{1}{2})}{\sqrt{\pi Q}}\exp\left\{-2\left[\frac{b}{\omega_0}-s(n+\frac{1}{2})\right]^2\right\}\left[(1-\cos 2\phi_0)+\frac{1}{16Q}(1+15\cos 2\phi_0)+O\left(\frac{1}{Q^2}\right)\right], \quad \text{(A.27)}$$

and

$$\sigma_n^{TM} = \frac{4s^2(n+\frac{1}{2})}{\sqrt{\pi Q}} \exp\left\{-2\left[\frac{b}{\omega_0} - s(n+\frac{1}{2})\right]^2\right\}\left[(1+\cos 2\phi_0) + \frac{1}{16Q}(1-15\cos 2\phi_0) + O\left(\frac{1}{Q^2}\right)\right], \quad \text{(A.28)}$$

Eq A.27 and A.28 includes an explicit information that most efficient excitation of TE- and TM-polarized resonances depends on the beam position such that TE-polarized resonances are most efficiently excited when the sphere is illuminated with a beam on the x-axis ($\phi_0 = 90^o, 270^o$) and TM-polarized resonances are most efficiently excited when the sphere is illuminated with a beam on the y-axis ($\phi_0 = 0^o, 180^o$).

VITA

Abdullah Demir completed the high school in Mühittin Güzelkılıç Lisesi, Konya, Turkey, in 1997. He received his B. Sc. degree in Physics from Koç University, Istanbul, Turkey, in 2002. He worked on the theory of high temperature superconductors as his undergraduate Independent Study. After a year in the Physics Engineering Department of Istanbul Technical University (ITU), he joined the M. Sc. program in Computational Science and Engineering of Koc University, in 2003, as a teaching/research assistant during which he has worked on "Elastic Scattering of Gaussian Beams from Microspheres". He will continue his Ph.D. work at University of Central Florida (UCF), College of Optics and Photonics (CREOL) in Orlando, Florida.

List of Publications:

1. Y.O. Yilmaz, A. Demir, A. Kurt, and A. Serpengüzel, "Optical Channel Dropping with a Silicon Microsphere," IEEE Photon. Technol. Lett. 17, 1662-1664 (2005).
2. A. Demir and A. Serpengüzel, "Silica Microspheres for Biomolecular Detection Applications," IEE Proceedings on Nanobiotechnology 152, 105-107 (2005). doi:10.1049/ip-nbt:20045010
3. A. Serpengüzel, A. Demir, and A. Kurt, "Semiconductor and Dielectric Microsphere based Channel Dropping Filters and Detectors," Proceedings of the Society of Photo-Optical Instrumentation Engineers Symposia: "Conference on Photonics and Optoelectronics," part of SPIE´s Second International Symposium on Microtechnologies for the New Millennium, Sevilla, Spain (May 9-11, 2005) ***(****Invited Paper****)***.
4. A. Serpengüzel, Y. O. Yilmaz, A. Demir, and A. Kurt, "Optical Resonances in Semiconductor Microspheres," Proceedings of the Society of Photo-Optical Instrumentation Engineers Symposia: Optics and Photonics in Security and Defence," London, UK (October 25-29, 2004).
5. A. Serpengüzel and A. Demir, "Laser Remote Sensing of Chemical Species," Advanced Technologies in Aviation Symposium, Airforce Academy, Yesilyurt, Istanbul, Turkey (December 9-10, 2004).

BIBLIOGRAPHY

[1] K. J. Vahala, Ed., *Optical Microcavities* (World Scientific, Singapore, 2004).

[2] K. J. Vahala, "Optical Microcavities", *Nature* 424, 839-846 (2003).

[3] A. A. Savchenkov, V. S. Ilchenko, A. B. Matsko, and L. Maleki, "Kilohertz optical resonances in dielectric crystal cavities", *Phys. Rev. A* 70, 051804(R) (2004).

[4] M. Cai, O. Painter, and K. J. Vahala, "Fiber-coupled microsphere laser," *Opt. Lett.* 25, 1430-1432 (2000).

[5] T. Bilici, S. Isci, A. Kurt, and A. Serpengüzel, "Microsphere-based channel dropping filter with an integrated photodetector," *IEEE Photon. Technol. Lett*. 16, pp. 476-478 (2004).

[6] M. Cai, G. Hunziker, and K. Vahala, "Fiber optic add-drop device based on a silica microsphere-whispering gallery mode system," *IEEE Photon. Technol. Lett.* 11, 686-687 (1999).

[7] H.C. Tapalian, J.P. Laine, and P.A. Lane, "Thermooptical switches using coated microsphere resonators," *IEEE Photon. Technol. Lett.* 14, 1118-1120, Aug. 2002.

[8] I. Teraoka, S. Arnold, and F. Vollmer, "Perturbation approach to resonance shifts of whispering-gallery modes in a dielectric microsphere as a probe of a surrounding medium," *J. Opt. Soc. Am. B*, vol. 20, pp. 1937-1946, Sept. 2003.

[9] A. Demir and A. Serpengüzel, "Silica microspheres for biomolecular detection applications," *IEE Proc. Nanobiotech.* 152, 105-108, (2005).

[10] S. Arnold, M. Khoshima, I. Teraoka, S. Holler, and F. Vollmer., "Shift of whispering-gallery modes in microspheres by protein adsorption," Opt. Lett. 28, 272-274 (2003).

[11] J. P. Laine, H. C. Tapalian, B. E. Little, and H. A. Haus, "Acceleration sensor based on high-Q optical microsphere resonator and pedestal antiresonant reflecting waveguide coupler," Sensors and Actuators A, vol. 93, 1-7 (2001).

[12] A. B. Matsko, A.A. Savchenkov, V.S. Ilchenko, and L. Maleki, "Optical gyroscope with whispering gallery mode optical cavities," *Opt. Commun.*, vol. 233, pp. 107–112 (2004).

[13] R.K. Chang and A. J. Campillo, Eds., Optical Processes in Microcavities (World Scientific, Singapore, 1996).

[14] S. M. Spillane, J.T. Kippenberg, and K. J. Vahala, "Ultralow threshold Raman laser using a spherical dielectric microcavity," *Nature* 415, 621-623 (2002).

[15] Y. O. Yilmaz, A. Demir, A. Kurt, and A. Serpengüzel, "Optical Channel Dropping with a Silicon Microsphere," *Photon. Technol. Lett.* 17, 1662-1664, August 2005.

[16] C. L. Baird and D. G. Myszka, "Current and emerging commercial optical biosensors," J. Mol. Recognit. 14, pp. 261–268, (2001).

[17] V. L. Seguin and S. Haroche, "Towards cavity-QED experiments with silica microspheres," Mater. Sci. Eng. 48 (1-2), pp. 53-58 (1997).

[18] S. Arnold, M. Khoshima, I. Teraoka, S. Holler, and F. Vollmer, "Shift of whispering-gallery modes in microspheres by protein adsorption," Opt. Lett. 28, pp. 272.274, (2003).

[19] F. Vollmer, D. Braun, A. Libchaber, M. Khoshsima, I. Teraoka, and S. Arnold, "Protein detection by optical shift of a resonant microcavity," Appl. Phys. Lett. 80, pp. 4057.4059, (2002).

[20] F. Vollmer, S. Arnold, D. Braun, I. Teraoka and A. Libchaber, "Multiplexed DNA Quantification by Spectroscopic Shift of Two Microsphere Cavities," Biophysical Journal 85, pp. 1974-1979, (2003).

[21] V. Lefevre-Seguin and S. Haroche, "Towards cavity-QED experiments with silica microspheres," Mater. Sci. Eng. B 48, 53–58 (1997).

[22] J. A. Lock, "Excitation efficiency of a morphology-dependent resonance by a focused Gaussian beam," J. Opt. Soc. Am. A 15, 2986-2994 (1998).

[23] D. S. Langley and M. J. Morrell, "Rainbow-enhanced forward and backward glory scattering," Appl. Opt. 30, 3459-3467 (1991).

[24] J. M. Vaughan, *The Fabry-Perot interferometer : history, theory, practice, and applications* (Adam Hilger, Bristol, England, 1989).

[25] M. Born and E. Wolf, Principles of Optics (Cambridge University Press, New York, 1999).

[26] L. Rayleigh, "The problem of the whispering gallery," Scientific Papers 5, 617 (1912).

[27] L. G. Guimardes and H. M. Nussenzveig, "Theory of Mie resonances and ripple fluctuations," Opt. Commun. 89, 363-369 (1992).

[28] E. Wolf, Ed., *Progress in Optics*, v. 41, (Elsevier, Netherlands, 2000).

[29] P. W. Barber, and R. K. Chang, *Optical Effects Associated with Small Particles* (World Scientific, Singapore, 1988).

[30] H.C. van de Hulst, Light Scattering by Small Particles (Dover, New York, 1981).

[31] C. F. Bohren and D. R. Huffman, *Absorption and Scattering of Light by Small Particles* (Interscience, New York, 1983).

[32] P. Barber, and S. C. Hill, *Light Scattering by Particles: Computational Methods* (World Scientific, Singapore, 1990).

[33] P. Guillon and Y. Garault, "Accurate Resonant Frequencies of Dielectric Resonators", *IEEE Transactions on Microwave Theory and Techniques*, Vol. MTT-25, No. 11, pp. 916-922, November 1977.

[33] M. L. Gorodetsky, A. A. Savchenkov, and V. S. Ilchenko, "Ultimate Q of optical microsphere resonators," *Optics Letters* 21, 453-455 (1996).

[34] P. Chylek, "Resonance structure of Mie Scattering: distance between resonances," *J. Opt. Soc. Am. A* 7, 1609-1613 (1990).

[35] B. E. Little, J. P. Laine, and H. A. Haus, "Analytic theory of coupling from tapered fibers and half-blocks into microsphere resonators." Journal of Lightwave Technology 17, 704-715, 1999.

[36] C. C. Lam, P. T. Leung, and K. Young, "Explicit asymptotic formulas for the positions, widths, and strengths of resonances in mie scattering," J. Opt. Soc. Am. B 9, 1585–1592 (1992).

[37] P. Chylek, "Resonance structure of mie scattering: distance between resonances," J. Opt. Soc. Am. A 7, 1609 -1615 (1990).

[38] C. F. Bohren and D. R. Huffman*, Absorption and Scattering of Light by Small Particles*, (Wiley, New York, 1983).

[39] G. Gouesbet, B. Maheu, and G. Gréhan, "Light scattering from a sphere arbitrarily located in a Gaussian beam, using a Bromwich formulation," J. Opt. Soc. Am. A 5, 1427–1443 (1988).

[40] J. P. Barton, D. R. Alexander, and S. A. Schaub, "Internal Fields of a spherical particle illuminated by a tightly focused laser beam: Focal point positioning effects at resonance," J. Appl. Phys. 65, 2900-2906 (1989).

[41] G. Gouesbet, G. Grehan, and B. Maheu, "On the Generalized Lorenz-Mie Theory: First Attempt to Design a Localized Approximation to the Computations of the Coefficients g_n^m," J. Optics (Paris) 20, 31-43 (1989).

[42] J. A. Lock and G. Gouesbet, “Rigorous justification of the localized approximation to the beam shape coefficients in generalized Lorenz-Mie theory. I. On-axis beams,” J. Opt. Soc. Am. A 11, 2503-2515 (1994).

[43] G. Gouesbet and J. A. Lock, ‘‘Rigorous justification of the localized approximation to the beam shape coefficients in generalized Lorenz-Mie theory. II. Off-axis beams,’’ J. Opt. Soc. Am. A 11, 2516-2525 (1994).

[44] G. Griffel, S. Arnold, D. Taskent, A. Serpengüzel, J. Connolly, and N. Morris, “Morphology Dependent Resonances of a Microsphere, Optical Fiber System,” Opt. Lett. 21, 695-697 (1996).

[45] A. Serpengüzel, S. Arnold, and G. Griffel, “Excitation of Resonances of Microspheres on an Optical Fiber”, *Optics Letters* 20, 654-656 (1995).

[46] M. L. Gorodetsky and V. S. Ilchenko, ‘‘High-*Q* optical whispering gallery microresonators: precession approach for spherical mode analysis and emission patterns,’’ Opt. Commun. **113**, 133–143 (1994).

[47] J. C. Knight, G. Cheung, F. Jacques, and T. A. Birks, “Phase matched excitation of whispering gallery modes by a fiber taper,” *Opt. Lett.* 22, 1129-1131 (1997).

[48] G. Griffel, S. Arnold, D. Taskent, A. Serpengüzel, J. Connolly, and N. Morris, "Morphology Dependent Resonances of a Microsphere/Optical Fiber System," Opt. Lett. 21, 695-697 (1996).

[49] M. L. Gorodetsky and V. S. Ilchenko, “Optical microsphere resonators: optimal coupling to high-Q whispering-gallery-modes,” J. Opt. Soc. Am. B. 16, 147-154 (1999).

[50] B.E.Little, J. P. Laine, and H. A. Haus, “Analytic Theory of Coupling from Tapered Fibers and Half-Blocks in Microsphere Resonators,” J. Lightw. Tech. 17, 704-715 (1999).

[51] A. Lock and J. G. Gouesbet, “Rigorous justification of the localized approximation to the beam-shape coefficients in a generalized Lorenz-Mie Theory. I. On-Axis Beams,” J. Opt. Soc. Am. A 11, pp. 2503-2515, (1994).

[52] L. W. Davis, “Theory of electromagnetic beams,” Phys. Rev. A 19, 1177-1179 (1979).

[53] S. A. Schaub, J. P. Barton, and D. R. Alexander, “Simplified scattering coefficient expressions for a spherical particle located on the propagation axis of a fifth-order Gaussian beam,” Appl. Phys. Lett. 55, 2709-2711 (1989).

[54] J. P. Barton and D. R. Alexander, “Fifth-order corrected electromagnetic field components for a fundamental Gaussian beam,” J. Appl. Phys. 66, 2800-2802 (1989).

[55] J. A. Lock, “Improved Gaussian beam-scattering algorithm,” Appl. Opt. 34, 559-570 (1995).

[56] J. A. Lock, “Excitation efficiency of a morphology-dependent resonance by a focused beam,” J. Opt. Soc. Am. A 15, 2986-2994 (1998).

[57] A. Serpengüzel, S. Arnold, G. Griffel, and J. A. Lock, “Enhanced coupling to microsphere resonances with optical fibers,” *J. Opt. Soc. Am. B* 14, 790-795 (1997).

[58] J. A. Lock, “Excitation efficiency of a morphology-dependent resonance by a focused beam,” J. Opt. Soc. Am. A 15, 2986-2994 (1998).

[59] S. M. Spillane, T. J. Kippenberg, O. J. Painter, and K. J. Vahala, “Ideality in a Fiber-Taper-Coupled Microresonator System for Application to Cavity Quantum Electrodynamics,” Phys. Rev. Lett. 91, 043902 (2003).

[60] J. A. Adam, “The mathematical physics of rainbows and glories,” Physics Reports 356, 229-365 (2002).

[61] D. S. Langley and M. J. Morrell, “Rainbow-enhanced forward and backward glory scattering,” Appl. Opt. 30, 3459-3467 (1991).

[62] J. A. Lock, “Theory of observations made of high-order rainbows from a single water droplet,” Appl. Opt. 26, 5291-5298 (1987).

[63] C. L. Adler, J. A. Lock, J. Mullholland, B. Keating, and D. Ekelman, “Experimental observation of total-internal-reflection rainbows,” *Appl. Opt.* 42, 406-411 (2003).

[64] J. A. Lock, “Contribution of high order rainbows to the scattering of a Gaussian laser beam by a spherical particle,” *J. Opt. Soc. Am. A* 10, 693-706 (1993).

[65] C. L. Baird and D. G. Myszka, “Current and emerging commercial optical biosensors,” J. Mol. Recognit. 14, pp. 261–268, (2001).

[66] D. Bergstein et al., "Resonant Cavity Imaging Biosensor," IEEE Lightwave Technologies in Instrumentation & Measurement Conference 2004.

[67] V.L. Seguin and S. Haroche, “Towards cavity-QED experiments with silica microspheres,” Mater. Sci. Eng. 48 (1-2), pp. 53-58 (1997).

[68] F. Vollmer, D. Braun, A. Libchaber, M. Khoshsima, I. Teraoka, and S. Arnold, "Protein detection by optical shift of a resonant microcavity," Appl. Phys. Lett. 80, pp. 4057.4059, (2002).

[69] S. Arnold, M. Khoshima, I. Teraoka, S. Holler, and F. Vollmer, "Shift of whispering-gallery modes in microspheres by protein adsorption," Opt. Lett. 28, pp. 272.274, (2003).

[70] S. C. Ching, H. M. Lai, "Dielectric microspheres as optical cavities: Einstein a and b coefficients and level shifts," Journal of Optical Society of America A, Vol. 20, no. 2, pp. 312-316, 1987

[71] F. Vollmer, S. Arnold, D. Braun, I. Teraoka and A. Libchaber, "Multiplexed DNA Quantification by Spectroscopic Shift of Two Microsphere Cavities," Biophysical Journal 85, pp. 1974-1979, (2003).

[72] E. Krioukov, A. Driessen, D. J. W. Klunder, J. Greve, "Sensor based on an integrated optical microcavity," Opt. Lett. 27, 512-514, 2002.

[73] S. Arnold, M. Khoshsima, I, Teraoka, S. Holler, F. Vollmer, "Shift of whispering gallery modes in microspheres by protein adsorption," Optics Letters, Vol. 28, no. 4, pp. 272-274, 2003.

[74] F. Vollmer, D. Braun, A. Libchaber, M. Khoshsima, I. Teraoka, S. Arnold, "Protein detection by optical shift of a resonant cavity," Applied Physics, Vol. 80,l no. 21, pp. 4057-4059, 2002.

[75] F. Vollmer, S. Arnold, D. Braun, I. Teraoka, A. Libchaber, "Multiplexed DNA quantification by spectroscopic shift of two microsphere cavities," Biophysical Journal, Vol. 85, pp. 1974-1979, 2003.

[76] A. Serpengüzel, S. Arnold, G. Griffel, and J. A. Lock, "Enhanced coupling to microsphere resonances with optical fibers," J. Opt. Soc. Am. B 14 (4), pp. 790-795, (1997).

[77] S. Pellegrin, A. Kozhekin, A. Sarfati, V. M. Akulin, and G. Kurizki, "Mie resonance in dielectric droplets with internal disorder," Phys. Rev. A 63, 33814, (2001).

[78] A. Yariv, *Introduction to Optical Electronics* (1995).

[79] S. A. Schaub, J. P. Barton and D. R. Alexander, "Simplified scattering coefficient expressions for a spherical particle located on the propagation axis of a fifth-order Gaussian beam," Appl. Phys Lett.55, 2709-2711 (1989).

[80] J. A. Lock, "Excitation efficiency of a morphology-dependent resonance by a focused beam," J. Opt. Soc. Am. A 15, 2986-2994 (1998).